

## Diurnal Variations of Warm-Season Precipitation East of the Tibetan Plateau over China

XINGHUA BAO

*School of Atmospheric Sciences, Nanjing University, Nanjing, China, and Department of Meteorology,  
The Pennsylvania State University, University Park, Pennsylvania*

FUQING ZHANG

*Department of Meteorology, The Pennsylvania State University, University Park, Pennsylvania*

JIANHUA SUN

*Institute of Atmospheric Physics, Chinese Academy of Sciences, Beijing, China*

(Manuscript received 4 January 2011, in final form 26 February 2011)

### ABSTRACT

This study explores the diurnal variations of the warm-season precipitation to the east of the Tibetan Plateau over China using the high-resolution NOAA/Climate Prediction Center morphing technique (CMORPH) precipitation data and the Global Forecast System (GFS) gridded analyses during mid-May to mid-August of 2003–09. Complementary to the past studies using satellite or surface observations, it is found that there are strong diurnal variations in the summertime precipitation over the focus domain to the east of the Tibetan Plateau. These diurnal precipitation cycles are strongly associated with several thermally driven regional mountain-plains solenoids due to the differential heating between the Tibetan Plateau, the highlands, the plains, and the ocean. The diurnal cycles differ substantially from region to region and during the three different month-long periods: the pre-mei-yu period (15 May–15 June), the mei-yu period (15 June–15 July), and the post-mei-yu period (15 July–15 August).

In particular, there is a substantial difference in the propagation speed and eastward extent of the peak phase of the dominant diurnal precipitation cycle that is originated from the Tibetan Plateau. This diurnal peak has a faster (slower) eastward propagation speed, the more (less) coherent propagation duration, and thus covers the longest (shortest) distance to the east during the pre-mei-yu (post-mei-yu) period than that during the mei-yu period. The differences in the mean midlatitude westerly flow and in the positioning and strength of the western Pacific subtropical high during different periods are the key factors in explaining the difference in the propagation speed and the eastward extent of this dominant diurnal precipitation cycle.

### 1. Introduction

The diurnal cycle of precipitation plays an important role in the local weather and climate (Dai 2001; Yang and Slingo 2001; Liang et al. 2004). The diurnal variations of precipitation are often induced by differential diabatic heating between regions with different surface topography including the contrast between mountains and plains and/or between land and sea. Recent studies have examined the diurnal variations of precipitation over

several mountain ranges and adjacent plains or basins over different continents (e.g., Carbone et al. 2002; Wang et al. 2004, 2005; Yu et al. 2007a,b; Fitzjarrald et al. 2008; Levizzani et al. 2010; Huang et al. 2010; He and Zhang 2010, hereafter HZ10). Many of these studies have found that the warm-season rainfall often generates over the highlands in the local midafternoon hours and then propagates<sup>1</sup> eastward or southeastward to adjacent lowlands in the night or early morning such as over North America

Corresponding author address: Dr. Fuqing Zhang, Department of Meteorology, The Pennsylvania State University, University Park, PA 16802.

E-mail: fzhang@psu.edu

<sup>1</sup> In this study, propagation is loosely defined as the speed of movement in space with time of a feature such as the peak or the minimum that includes pure translation in space and mean flow effect.

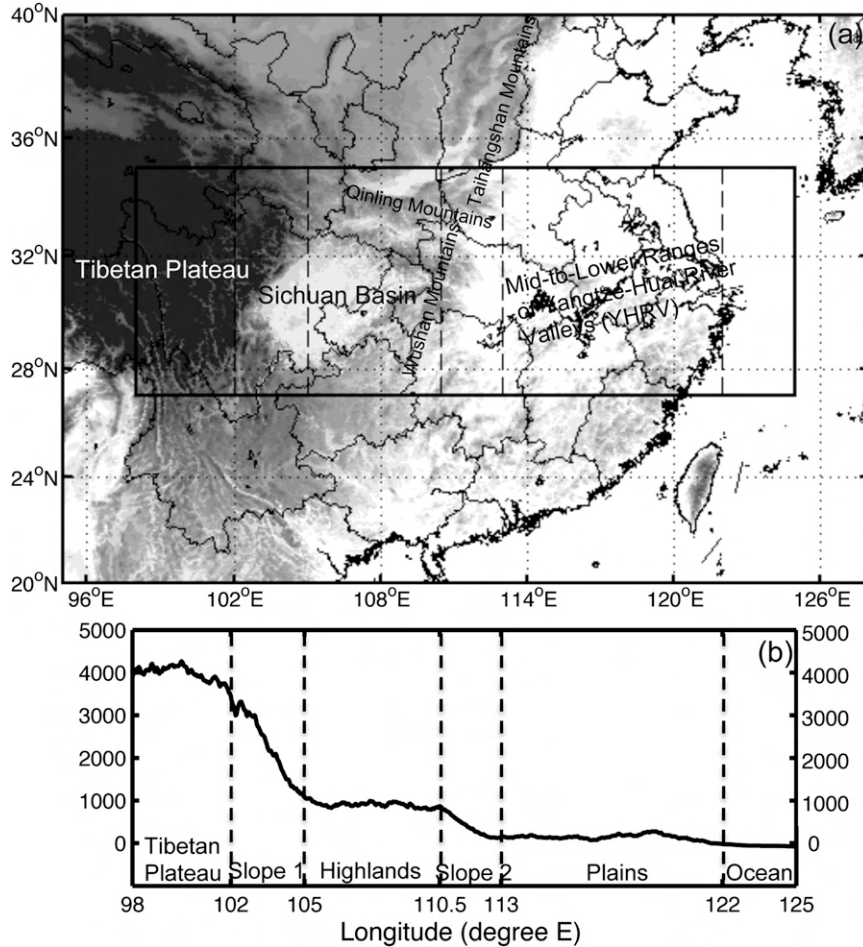


FIG. 1. (a) Map of terrain elevations (shaded every 250 m) over China with the focus domain ( $27^{\circ}$ – $35^{\circ}$ N,  $98^{\circ}$ – $125^{\circ}$ E) highlighted in the black rectangle. (b) The average terrain elevations (m) along the west–east cross section in the focus domain with characteristic terrain types separated by black dashed lines.

(Carbone et al. 2002) and East Asia including different regions of China (Wang et al. 2004, 2005; Yu et al. 2007a,b; Huang et al. 2010; HZ10). Carbone et al. (2002) suggest that the fixed timing, areal coverage, and longevity of these diurnal precipitation cycles may be potentially used to extend the predictability of the warm-season rainfall forecasts if these diurnal cycles can be properly captured in numerical weather prediction models.

The terrain elevations over China change drastically from the high Tibetan Plateau (TP) on the west to highlands in the middle and the low-lying plains on the east (Fig. 1a). The strong contrast in terrain elevations is responsible for the occurrence of warm-season diurnal precipitation cycles (Wang et al. 2004, 2005; Chen et al. 2010). The vast majority of areas in China east of the TP are under the influence of the East Asia summer monsoon with the primary monsoon rain belt advancing northward

from mid-May to mid-August (Tao and Chen 1987). The TP and other mountain ranges are important factors in organizing and modulating precipitation during the Asian summer monsoon period (Xie et al. 2006). The dual influence of complex topography and the summer monsoon on the diurnal variations of warm-season precipitation over this region has been noted in many recent studies (e.g., Geng and Yamada 2007; Wang et al. 2004, 2005; Yu et al. 2007a,b; Chen et al. 2009; Chen et al. 2010). Some of these studies also examined the regional difference of diurnal precipitation variations and propagation (e.g., Wang et al. 2004, 2005; Hirose and Nakamura 2005). Most recently, through the case study of an individual episode on the lee side of TP, Huang et al. (2010) found that a solenoidal circulation between TP and its leeside lowlands contributes to the longevity and farther downstream propagation of the diurnal precipitation peak.

Some studies also examined the diurnal variations of precipitation over East Asia over one or several subperiods of the warm season (Asai et al. 1998; Chen et al. 2009; Xu and Zipser 2011). Under the monsoon influence, climatologically the primary rain belt over China moves from south to north with the rainy season in south China during mid-May and mid-June, the mei-yu season in the Yangtze-Huai River Valleys (YHRV) of central and east China during mid-June and mid-July, and the rainy season in north China during mid-July and late August. According to the climatological mean positions of the primary rainband, the current study divides the warm season in the focus domain (areas east of TP over China) into three periods: the pre-mei-yu period (15 May–15 June), the mei-yu period (15 June–15 July), and the post-mei-yu season (15 July–15 August).

Complementary to past studies, which mostly analyzed the characteristics of the diurnal precipitation cycle on the entire warm season, this study explores the diurnal variations in the warm-season precipitation to the east of the TP over China with a focus on the difference during three different month-long periods, each of which represents a different rainy season in China. Section 2 provides a description of the dataset and methodology. Section 3 describes the overview of the warm-season precipitation east of the TP over China. Characteristics and the variations in the diurnal precipitation, along with the connection with several regional mountain–plains solenoidal circulations, are examined in section 4. Section 5 discusses the difference in diurnal variation during different periods. Conclusions are given in section 6.

## 2. Data and methodology

As in HZ10, the high-resolution global precipitation dataset from the National Oceanic and Atmospheric Administration (NOAA) Climate Prediction Center (CPC) morphing technique (CMORPH; Joyce et al. 2004) is used for this study. Seven warm seasons of the CMORPH dataset during 2003–09 (mid-May to mid-August) will be examined. The CMORPH has a spatial resolution of  $0.072^{\circ} \times 0.072^{\circ}$  available every 30 min between  $60^{\circ}\text{N}$  and  $60^{\circ}\text{S}$  produced since December 2002. It combines precipitation estimates derived exclusively from several low-orbit satellite microwave sensors. The CMORPH dataset uses the spatial propagation information that is obtained from geostationary satellite infrared data to transport the microwave-derived precipitation features during periods when microwave data are not available at a location. Recently, Shen et al. (2010) compared the spatial distribution and seasonal variations of 6 satellite-based precipitation estimates, including CMORPH, with over 2000 rain gauge measurements during 2005–07. They found the CMORPH

rainfall estimates had the best agreement with the rain gauge observations, especially during warm-season months (May–August) over east and south China. They also found that the CMORPH dataset depicted well the diurnal variations and propagation of the warm-season precipitation, despite some underestimation of early morning rainfall maxima over the plains. The reliability of the CMORPH dataset on warm-season and annual rainfall estimation has also been demonstrated in several other recent studies (Fitzjarrald et al. 2008; Hirpa et al. 2010; Pereira Filho et al. 2010).

Besides the CMORPH dataset, the NOAA Global Forecast System (GFS)  $1^{\circ} \times 1^{\circ}$  operational analyses every 6 h over the same period are used to provide the corresponding environmental conditions. Our analysis domain is over a  $33^{\circ} \times 20^{\circ}$  longitude–latitude domain ( $20^{\circ}$ – $40^{\circ}\text{N}$ ,  $95^{\circ}$ – $128^{\circ}\text{E}$ ; Fig. 1a) that covers most areas of China with the focus area on a  $27^{\circ} \times 8^{\circ}$  to the east of the TP including the Sichuan basin sandwiched by the Qinling and Wushan Mountain ranges, as well as the low-lying mid- to lower ranges of the YHRV and the adjacent oceans. The focus area is home to more than a third of China's population that includes several of the most populous provinces and cities in China. On average, the terrain elevation decreases from west to east (Fig. 1b). The latitude-averaged highest step of the TP has mean elevations above 3500 m. The second step is the highlands in southwest and central China that includes the Sichuan basin and the surrounding mountain ranges (hereafter refer to as “the highlands”) with average elevations  $\sim 1000$  m. The third step is the plains over central and east China along the mid- to lower ranges of the YHRV (hereafter referred to as “the plains”) that have average terrain elevation less than 300 m with the ocean to the east.

To highlight the larger-scale variations in the diurnal precipitation cycles and to directly compare with a coarse GFS analysis, as in HZ10, this study also uses a two-dimensional spectral decomposition technique developed in Lin and Zhang (2008) to truncate signals with horizontal scales less than 300 km. The spectral filtering is performed on the latitude–longitude grid over the entire domain of Fig. 1a though only plotted in a subset of this domain in subsequent figures.

## 3. Overview of warm-season precipitation in the focus domain

The warm-season precipitation (mid-May through mid-August) accounts for most of the annual rainfall in China with the highest amount over south China and gradually decreasing to the north and west (Fig. 2a). Accompanied by the northward progression of the East Asian summer monsoon, there are three distinguished

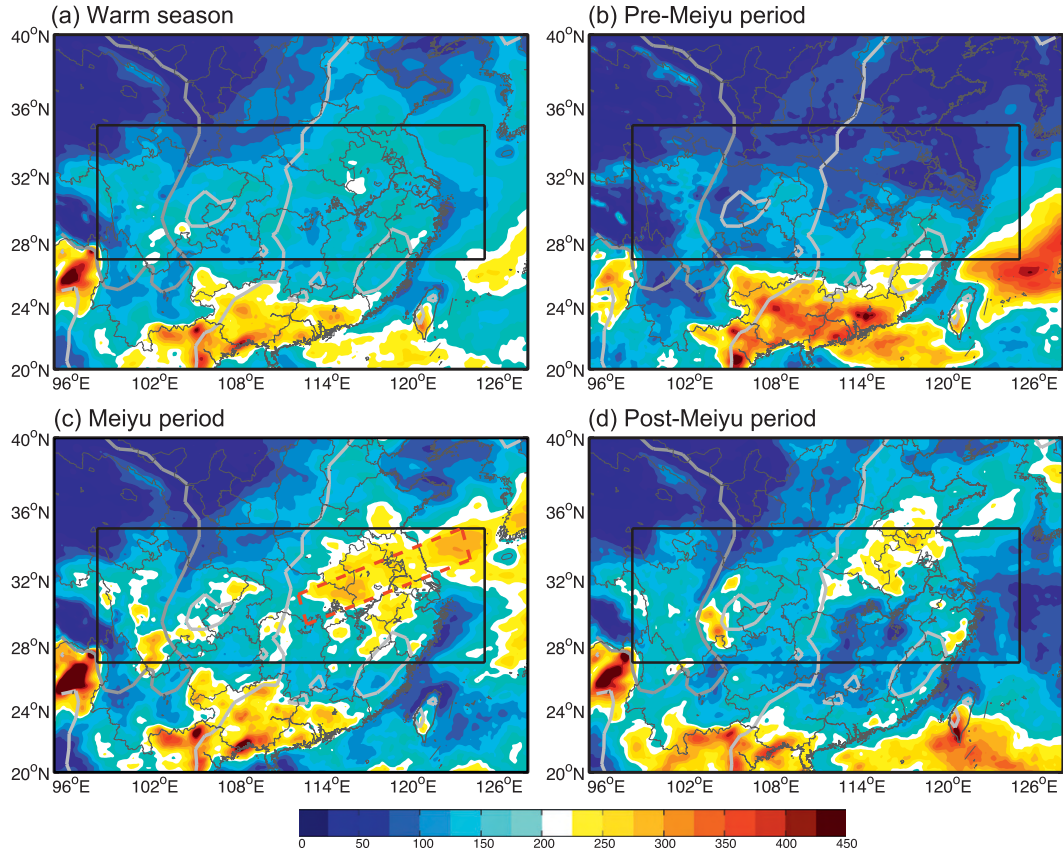


FIG. 2. Distribution of mean monthly total precipitation (mm) during (a) the entire warm season, (b) the pre-meyu period, (c) the mei-yu period, and (d) the post-meyu period averaged over all hours during 2003–09 estimated with the CMORPH dataset. The bold lighter gray lines denote the terrain elevation of 500 m, and the bold darker gray lines denote the elevation of 2000 m. These two terrain contours mark the approximate locations of the two steepest terrain slopes, slope 1 and slope 2, marked in Fig. 1b, respectively. The red dashed box in (c) denotes the primary meiyu front rain belt during the meiyu period.

phases of warm-season precipitation with quasi-stationary rainfall belts on average situated over south China during mid-May to mid-June, over mid- to lower ranges of the YHRV in central and east China during mid-June to mid-July, and over north China from mid-July to mid-August (Tao 1980; Tao and Chen 1987).

The northward movement of the quasi-stationary quasi-linear east–west-oriented rain belt is strongly linked to the position and strength of the western Pacific subtropical high (WPSH) and the midlatitude westerly flow (Fig. 3). The quasi-stationary rain belt over the focus domain during mid-June to mid-July is typically called the meiyu season in this area.<sup>2</sup> For simplicity, this study will characterize the duration between 15 May and 15 June

as the pre-meyu period, between 15 June and 15 July as the meiyu period, and between 15 July and 15 August as the post-meyu period over the focus area to the east of the TP over China. Given strong differences in the climatological mean of the synoptic environment for these three different periods (Figs. 3b–d), this study will examine the changes in the diurnal variations of precipitation over these three different warm-season periods over the focus domain. This will complement past studies of the diurnal variations in precipitation over this area that focused broadly over the entire summer seasons (e.g., Wang et al. 2005; Yu et al. 2007a,b) or exclusively over the meiyu season (e.g., Geng and Yamada 2007). Moreover, this study will also seek to understand the similarities and differences in propagation and diurnal variation mechanisms during different rainfall periods.

From the CMORPH dataset averaged over 2003–09, the maximum monthly mean precipitation totals of 250–450 mm are located over south China (south of 27°N

<sup>2</sup> Mei-yu is also called baiyu in Japan and sometimes may refer broadly to all quasi-stationary precipitation belts associated with the East Asian summer monsoon during all warm seasons.

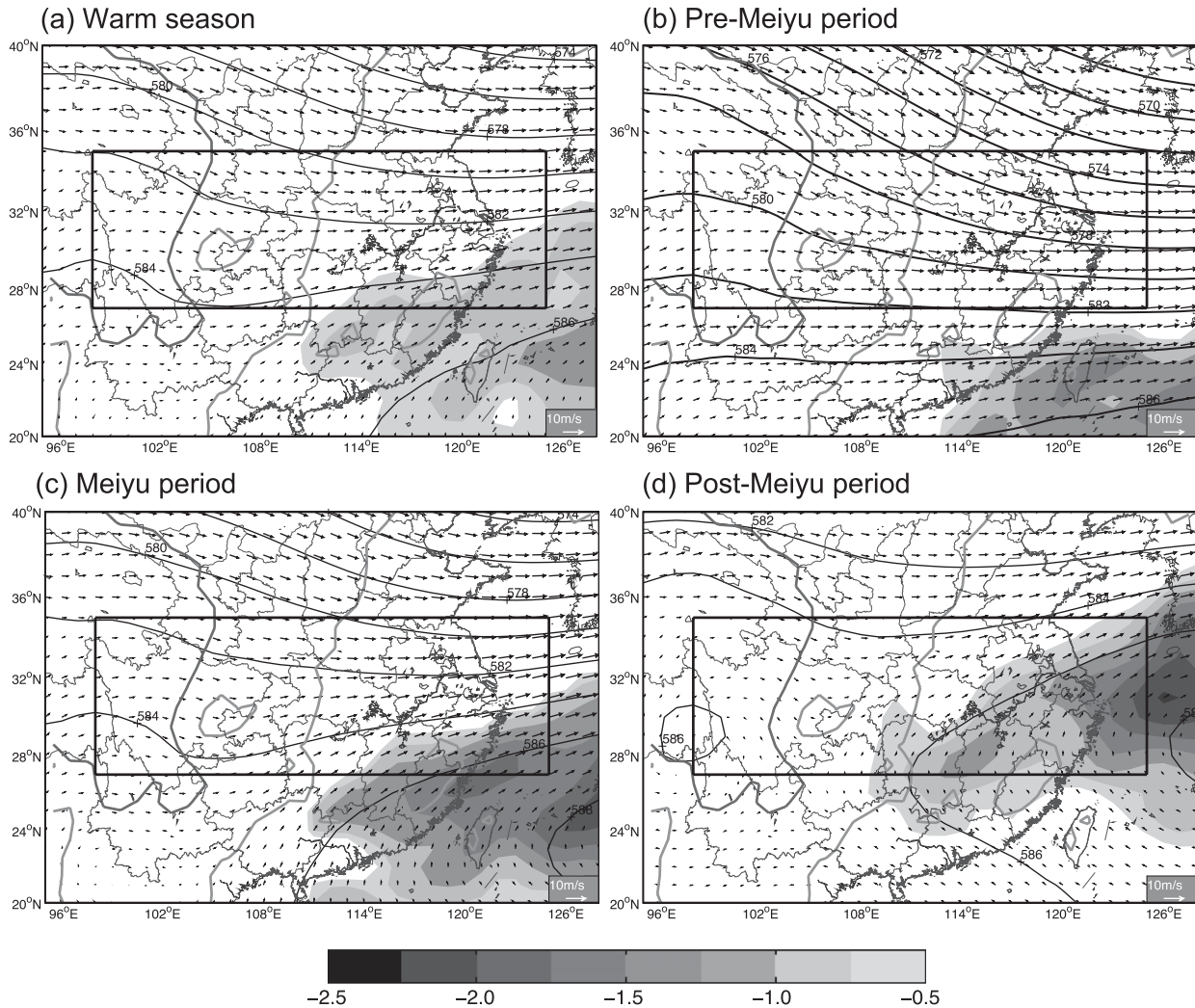


FIG. 3. Spatial distribution of the 500-hPa horizontal wind vectors, geopotential height (2-dam intervals) and negative vorticity (shaded,  $10^{-5} \text{ s}^{-1}$ ) averaged over (a) the entire warm season, (b) the pre-mei-yu period, (c) the mei-yu period, and (d) the post-mei-yu period.

outside of the focus domain) during the pre-mei-yu period (15 May–15 June). Within the focus domain, local maxima with monthly total precipitation between 100 and 200 mm are observed in the eastern edge of the TP, as well as over the highlands east of the Sichuan basin and the southern portion of the east China plains (Fig. 2b). During the mei-yu period (15 June–15 July), although precipitation over south China especially along the coastal areas remains strong (but weakened compared to the pre-mei-yu period), nearly all areas in the focus domain encounter increased precipitation. The primary rain belt with monthly total maxima over 300 mm moves over to the east China plains along the mid- to lower ranges of the YHRV oriented mostly along the west-east direction (Fig. 2c). During the post-mei-yu period, this primary rain belt continues moving northward to the

north China plains across the northern boundary of the focus domain while rainfall decreases substantially along the YHRV over most of the southern half of the focus domain (Fig. 2d).

Differences in the large-scale flow regimes and weather patterns not only leads to large differences in the amount and distribution of the precipitation in the focus domain during different periods, but also results in significant differences in the diurnal variations and propagation of the rainfall as evidenced from the averaged plots in Fig. 4 and the time-longitude Hovmöller diagrams in Fig. 5 for different periods. Figure 4 shows the spatial distribution of the diurnal percentage of the total precipitation during different periods over the focus domain and surrounding areas. As in HZ10, the diurnal percentage (DP) is defined as

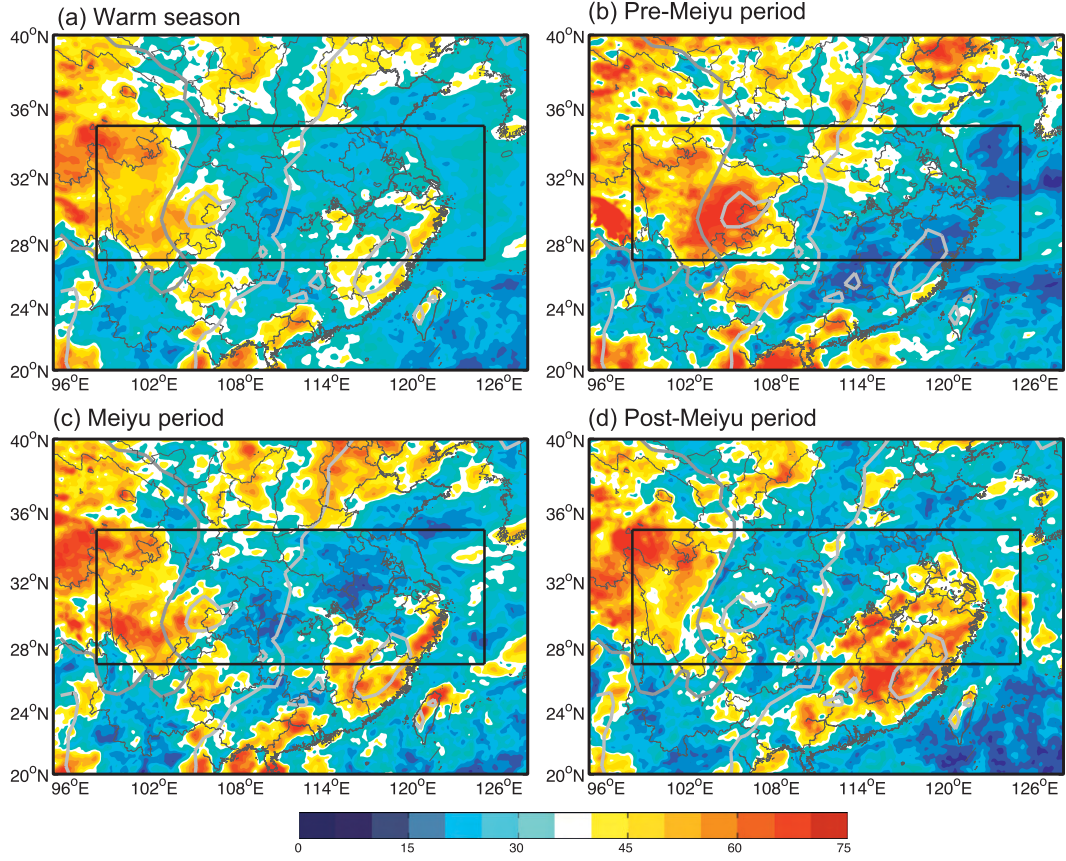


FIG. 4. Percentage (%) of the diurnal contributions of the total precipitation averaged over (a) the entire warm season, (b) the pre-mei-yu period, (c) the mei-yu period, and (d) the post-mei-yu period.

$$DP = \frac{\sum_{t=1}^{24} |(r_t - \bar{r})|}{r_d}. \quad (1)$$

Here,  $r_t$  is the mean precipitation rate at each hour,  $\bar{r}$  is the mean hourly precipitation rate, and  $r_d$  is the mean daily precipitation.

Different from the total rainfall distribution in Fig. 2a, the highest percentage in diurnal precipitation with values between 30% and 50% occurs on the eastern TP including the adjacent sharpest terrain slope and the Sichuan basin to the east; the diurnal percentage of precipitation drops to below 20% for most of the high and low plains to the east except for the mountainous areas in the southeast edge of the focus domain (Fig. 4a). The distribution of the diurnal precipitation percentage varies from period to period, with the mei-yu period most similar to the warm-season average (Fig. 4c). Among the three warm-season months, the pre-mei-yu (post-mei-yu) period has the highest (lowest) diurnal percentage over the Sichuan basin but the lowest (highest) on the plains (Figs. 4b,d).

It is worth noting that our definition of DP includes the variations of precipitation during different hours of the day besides the pure diurnal cycle, which differs from a more strict definition used in Carbone and Tuttle (2008). The DP calculation using their definition yields similar distribution patterns as in Fig. 4 (not shown) though the absolute percentage value is smaller without higher-frequency modes.

Following the methodology of Fig. 12 of Carbone et al. (2002) and Fig. 4 of HZ10, Fig. 5a shows the longitude-time Hovmöller diagram of the normalized hourly precipitation deviations averaged along the cross section from west to east. The map distributions of the normalized hourly precipitation deviations at different hours are shown in Fig. 6. Precipitation over the eastern TP shows obvious characteristics of diurnal variations with a dominant peak in the afternoon hours (around 0900–1200 UTC or 1700–2000 BJT;<sup>3</sup> Figs. 5a and 6d,e) and a minimum in

<sup>3</sup> Note that the local standard time (LST) over areas east of TP is within 2 h of Beijing standard time (BJT). BJT is 8 h ahead of the coordinated universal time (UTC).

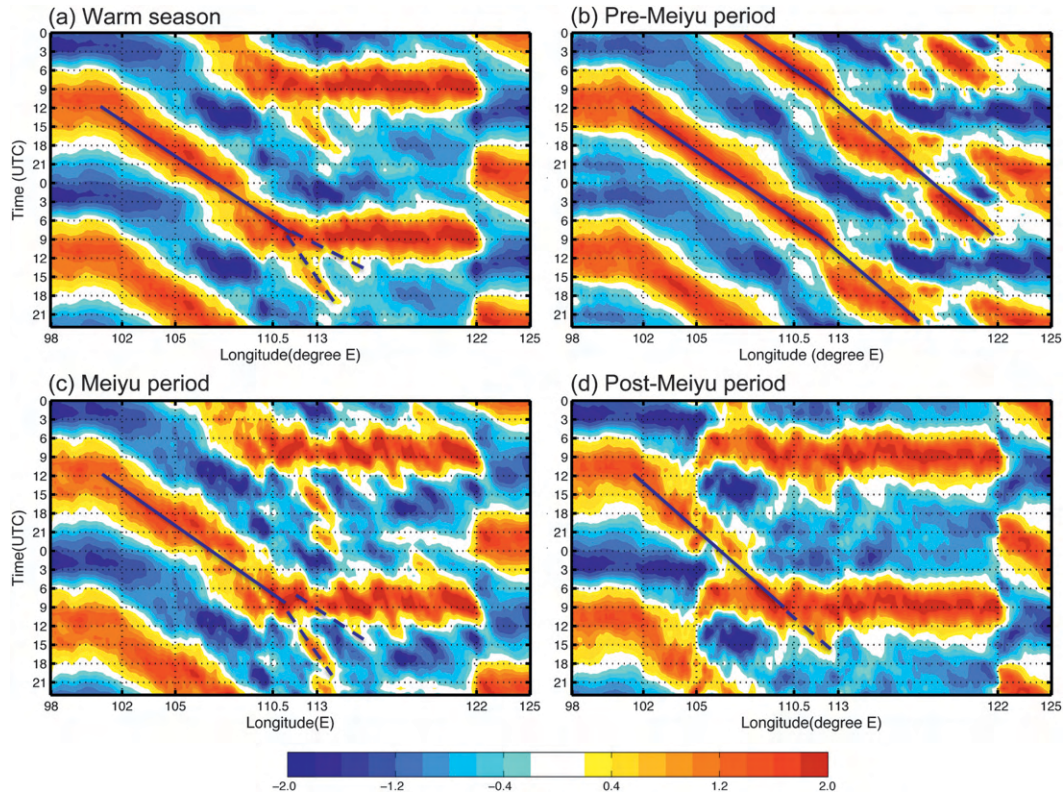


FIG. 5. Longitude–time Hovmöller diagrams of the normalized hourly precipitation deviation without filtering averaged from 27° to 35°N and over (a) the entire warm season, (b) the pre-mei-yu period, (c) the mei-yu period, and (d) the post-mei-yu period. The solid lines denote the eastward propagation of the primary coherent diurnal precipitation peak while the dashed lines denote other secondary or less-coherent eastward-propagation modes.

the morning (around 0000–0300 UTC or 0800–1100 BJT; Figs. 5a and 6a,b). The maximum diurnal precipitation peak over the TP (near 100°E) begins to migrate eastward and downslope around 1200 UTC (2000 BJT; Figs. 5a and 6e) starting from around 102°E that arrives at the highlands (near 105°E) around 1500–2100 UTC (2300–0500 BJT; Figs. 5a and 6f–h). The maximum rainfall in the Sichuan basin area occurs mainly in the nighttime and early morning hours (nocturnal) consistent with previous studies (Wang et al. 2004; Kurosaki and Kimura 2002). The diurnal precipitation maximum continues moving eastward at a similar phase speed ( $\sim 13 \text{ m s}^{-1}$ ), but gradually slows and weakens in relative magnitude that coexists and may interact with other diurnally varying precipitation modes. The dominant diurnal precipitation peak persistent over all land areas to the east of 108°E occurs between 0700 and 1000 UTC (or 1500–1800 BJT, midafternoon) while a secondary propagating maximum, as a continuation of the signal from the TP and the Sichuan basin, peaks at approximately 1500–1800 UTC (or 2300–0200 BJT, around midnight the second day) between 112° and 114°E.

Farther eastward propagation of this diurnal peak is hard to track east of 115°E in the latitudinal average

(Fig. 5a) as the eastward-propagating diurnal peak interacts with other modes, resulting in a more complex diurnal precipitation variation pattern over the plains (Figs. 5a and 6). One such mode is the southeastward-propagating diurnal precipitation peak that originated from a northeast–southwest-oriented terrain slope between the mountain ranges and plains in north China (Figs. 6c–g), which was examined previously in HZ10. Another is a nonpropagating, quasi-stationary oscillatory mode typical of summertime precipitation over land that has a peak in the afternoon and a minimum in the morning. The nonpropagating oscillatory diurnal mode becomes the dominant signal over land east of 114°E in the latitudinal average of Fig. 5a, while the southeastward-propagating mode is most evident in the map plot of Fig. 6.

Over the ocean (east of 122°E), the diurnal cycle phase is nearly opposite to that over the land: there is a late night and early morning maximum (1800–0300 UTC or 0200–1100 BJT) and a late afternoon and early night minimum (0900–1500 UTC or 1700–2300 BJT; Fig. 5a). The late-evening to early-morning rainfall maximum over the ocean is consistent with past observational studies (e.g., Dai 2001; Yang and Smith 2006).

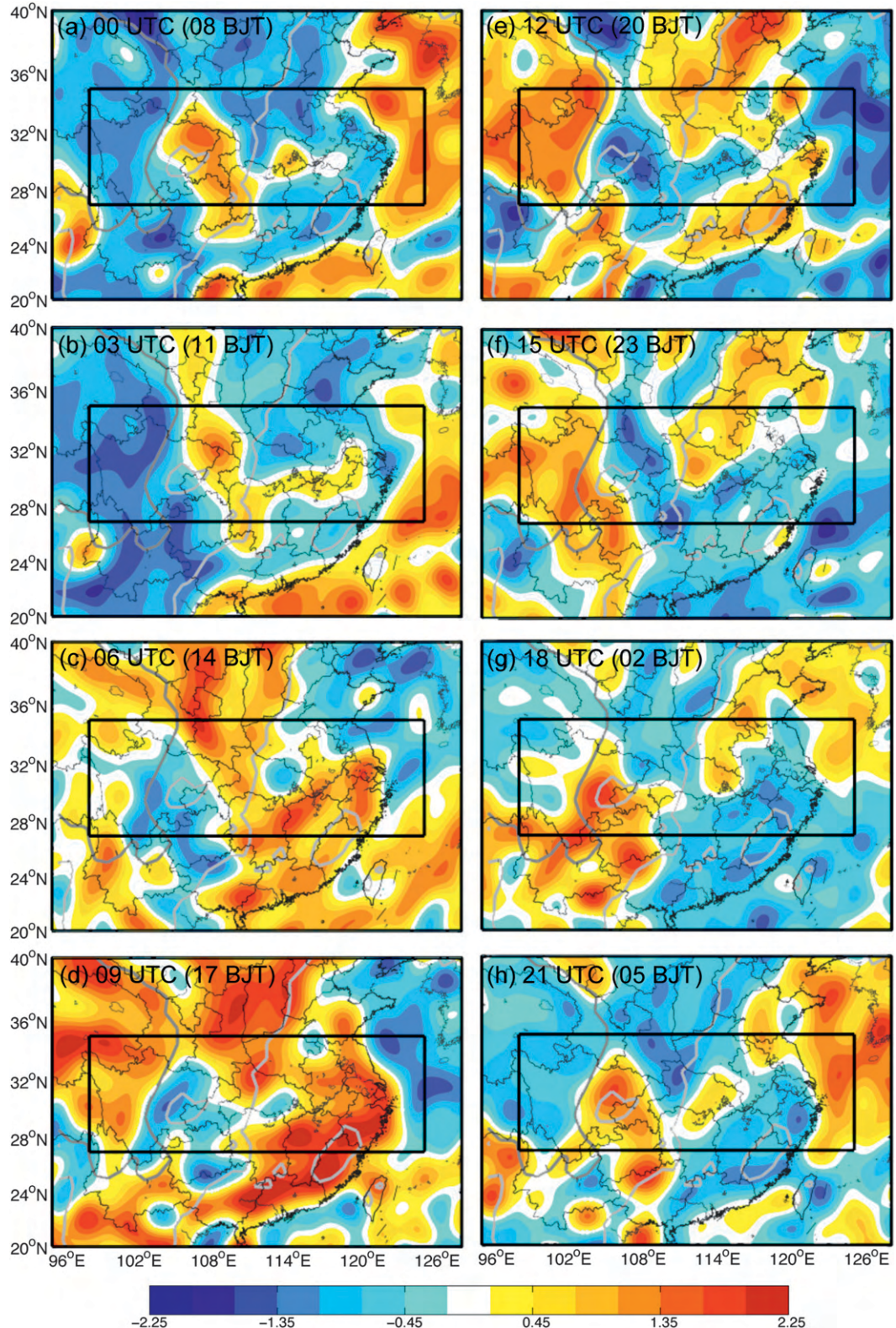


FIG. 6. Normalized diurnal precipitation deviations at (a) 0000, (b) 0300, (c) 0600, (d) 0900, (e) 1200, (f) 1500, (g) 1800, and (h) 2100 UTC averaged over the entire warm season. Scales smaller than 300 km are truncated by a 2D spectral decomposition technique as in Lin and Zhang (2008).

The diurnal evolution of summertime precipitation revealed from the CMORPH dataset in Fig. 5a is broadly consistent with Wang et al. (2004, 2005), who used hourly infrared (IR) brightness temperature derived from the Geostationary Meteorological Satellite (GMS). One noticeable difference between this study and Wang et al. (2004, 2005) is that the averaged eastward-propagation speed derived from the CMORPH dataset is  $\sim 13 \text{ m s}^{-1}$  and is slower than  $17 \text{ m s}^{-1}$  found in their study. This difference may be due to the difference in the averaging latitude range ( $20^\circ\text{--}40^\circ\text{N}$  vs  $27^\circ\text{--}35^\circ\text{N}$ ), the difference in the data sources (GMS satellite IR brightness temperature versus CMORPH rainfall), and/or the period of the dataset (1 May–31 August 1998–2001 vs 15 May–15 August 2003–09). Tuttle et al. (2008) noted that the infrared (IR)-based propagation speeds are on average  $\sim 4 \text{ m s}^{-1}$  faster than that of radar-measured speeds suggesting that the IR-based phase speeds are faster than the typical deep westerly shear.

The diurnal peak originating from the eastern edge of the TP has the fastest and most coherent propagation all the way to the east coast of China during the pre-mei-yu period (Fig. 5b). The WPSH is weak and farther south and east while the focus area is well within the midlatitude westerly flow at 500 hPa (Fig. 3b). The slowest and least coherent propagating diurnal precipitation peaks are observed during the post-mei-yu period that is confined mostly to the eastern slope of the TP and adjacent highlands (Fig. 5d), while most of the focus area is within the westward extent of the WPSH (Fig. 3d). The east China plains during this period are controlled mostly by the same phase nonpropagating diurnal variation that peaks in the late afternoon around 0900 UTC (1700 BJT; Fig. 5d). During the mei-yu period, the rainfall diurnal variation and propagation is the most complicated with the coexistence of both the stationary and eastward-propagating modes over the central and east China plains (Fig. 5c), while the focus area becomes the transition zone of the WPSH and the westerly flows (Fig. 3c).

Figure 7 shows the latitudinally averaged daily and diurnal rainfalls as well as the diurnal percentage of the daily rainfall averaged during different periods. As in Fig. 2, the averaged maximum rainfall is found in the mei-yu period, followed by the post-mei-yu period, and the lowest is during the pre-mei-yu period. There are two primary local rainfall maxima present in each of the three periods with the weaker and narrower peak located on the eastern edge of the TP and the stronger and broader peak on the plains between  $113^\circ\text{E}$  and  $122^\circ\text{E}$  (Fig. 7a). These two local maxima are most noticeable during the mei-yu period and least apparent during the pre-mei-yu period.

The diurnal percentage of the daily rainfall [defined in Eq. (1)], on the other hand, shows greater difference

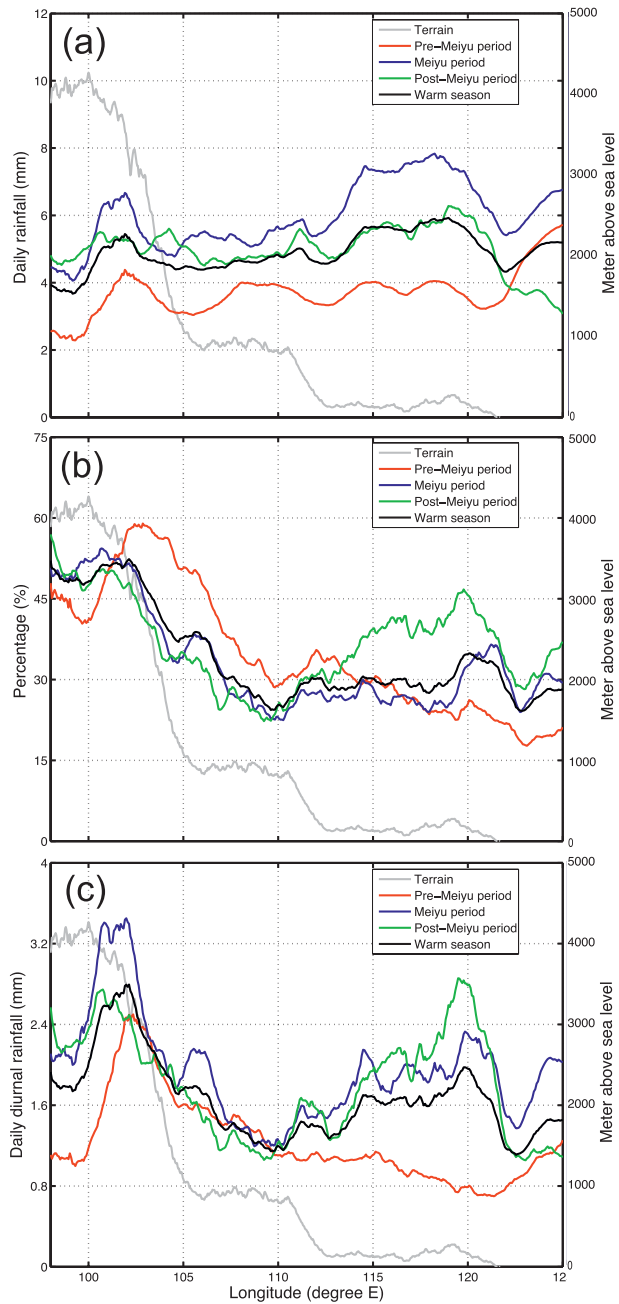


FIG. 7. Map plots of (a) the daily rainfall (mm), (b) the diurnal percentage of the daily rainfall (%), and (c) the daily diurnal rainfall (mm) latitudinally averaged from  $27^\circ$  to  $35^\circ\text{N}$  during different periods. The gray solid curves show the average terrain elevation (m).

from period to period, especially over the plains east of  $112^\circ\text{E}$  (Fig. 7b). During the pre-mei-yu period, the diurnal precipitation contributes as much as 60% on the lee slope of the TP (near  $102.5^\circ\text{E}$ ), which drops nearly linearly to  $\sim 30\%$  at  $110^\circ\text{E}$ . A secondary peak of  $\sim 35\%$  is observed at the second terrain slope ( $\sim 112^\circ\text{E}$ ) that

further declines over the east China plains and reaches less than 20% on the coast.

The latitudinally averaged diurnal percentage of the precipitation during the mei-yu and post-mei-yu periods west of  $113^{\circ}\text{E}$  (Fig. 7b) is more or less similar to the pre-mei-yu period though the primary peak on the eastern edge of TP becomes slightly weaker [ $\sim(50\%-55\%)$ ] and  $2\text{--}3^{\circ}$  more to the west along with a more noticeable enhancement at the foothills of TP (i.e., over the Sichuan basin and surrounding areas). Although the diurnal percentage increases at the second terrain slope ( $\sim 112^{\circ}\text{E}$ ) for both the mei-yu and post-mei-yu periods, there is no obvious secondary peak in this longitude range. The diurnal percentage over the plains east of  $112^{\circ}\text{E}$  stays at similar values between 25% and 30% until an enhancement to nearly 40% on the coastal area. The diurnal percentage during the post-mei-yu period, on the other hand, increases steadily over the plains from a minimum of  $\sim 25\%$  at  $110^{\circ}\text{E}$  to a peak above 45% on the coast (Fig. 7b). Correspondingly, the averaged daily diurnal rainfall during the pre-mei-yu period is similar to the mei-yu and post-mei-yu periods west of  $110^{\circ}\text{E}$  (over the TP and adjacent highlands) but significantly smaller over the plains east of  $110^{\circ}\text{E}$  (Fig. 7c).

To further elucidate the difference of total precipitation and the period-mean synoptic environment, sections 4a–c will examine separately the characteristics and dynamics of the summertime rainfall diurnal variations during each of the three periods.

#### 4. Diurnal variations of summertime precipitation during different periods

##### a. The pre-mei-yu period (15 May–15 June)

Figure 8 shows the normalized diurnal precipitation deviations at different hours during the pre-mei-yu period (15 May–15 June). As in HZ10, to highlight the larger-scale variations of the diurnal precipitation cycles and to directly compare with a coarse GFS analysis, a two-dimensional spectral decomposition (Lin and Zhang 2008) has been used to truncate signals with horizontal scales less than 300 km in Fig. 6 (as well as in Figs. 8, 11, and 14). Consistent with Fig. 5b, a diurnal precipitation peak starts at 0600 UTC (1400 BJT; Fig. 8c) over the eastern edge of the TP ( $98^{\circ}\text{--}100^{\circ}\text{E}$ ). The strongest diurnal peak is observed on the sharpest terrain slope east of the TP at 1500 UTC (2300 BJT; Fig. 8f). This diurnal peak subsequently moves downslope reaching the Sichuan basin ( $105^{\circ}\text{--}108^{\circ}\text{E}$ ) between 1800 and 2100 UTC (0200 and 0500 BJT; Figs. 8g,h) corresponding to the nocturnal and early morning rainfall maximum widely observed in this area. The peak phase continues moving eastward arriving

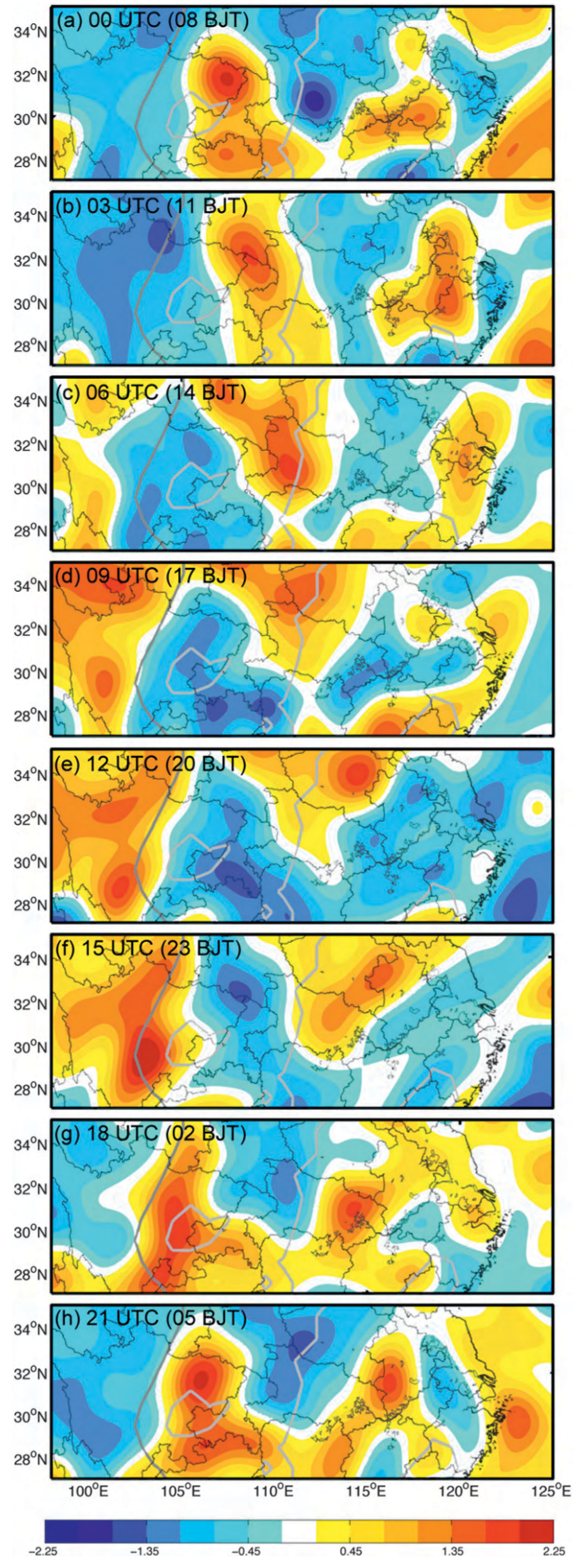


FIG. 8. As in Fig. 6, but for the pre-mei-yu period.

at the Qinling and Wushan Mountain ranges at 0600 UTC (1400 BJT; Fig. 8c) on the second day, which is locally enhanced near  $110^{\circ}$ – $112^{\circ}$ E as it moves down the eastern slope of these mountain ranges at around 0900 UTC (1700 BJT; Fig. 8d). The peak phase front becomes less north–south oriented and less coherent thereafter during its continuous eastward propagation reaching the east China plains in the later evening and early morning hours (1500–2100 UTC or 2300–0500 BJT; Figs. 8f–h) corresponding to another nocturnal precipitation maximum also well-observed in this area. The remnant of this diurnal peak has traceable eastward propagation even during the third day until it reaches the east coast, albeit even lesser coherent and weaker (Figs. 8a–c).

From the eastern edge of the TP to the coastal plains, this diurnal precipitation peak is clearly traceable for nearly 2 days with an average eastward-propagation speed of approximately  $15 \text{ m s}^{-1}$  (Fig. 5b). In general, the diurnal precipitation peaks in the afternoon hours on the high mountains or their eastern slopes and in the late evening or early morning on the plains or the basins. In addition, the diurnal peaks usually weaken as they propagate away from the terrain slopes suggesting the differential heating between highland and lowland (or between land and sea) is essential in controlling the diurnal cycles along with the influence of the large-scale environment.

As discussed in HZ10, the speed of phase propagation and the relationship between the local diurnal precipitation peak and minimum may be related to the diurnal variations of several regional-scale mountain–plains solenoid (MPS) circulations induced by differential heating between the plateaus, highlands, and plains over this region. Following HZ10, which focused on north China, this study examined the mean GFS analysis available every 6 h averaged through the warm-season months of 2003–09 as shown in Figs. 9 and 10 over the focus domain from the TP to the coastal plains. The evolution of the MPS circulation over many places of the world along with its impacts on summertime precipitation and other weather phenomena have been extensively studied (e.g., Tripoli and Cotton 1989; Dai et al. 1999; Zhang and Koch 2000; Koch et al. 2001; Carbone et al. 2002; Wang et al. 2004, 2005; Hirose and Nakamura 2005; Laing et al. 2008; Carbone and Tuttle 2008).

Figure 9 shows the low-level (850-hPa) vertical motion deviations and perturbation wind vectors of each GFS analysis during the pre-mei-yu period averaged over 2003–09. Figure 10 shows the corresponding latitudinally averaged vertical motions and the perturbation vertical circulation vectors along the west–east cross section. At 0600 UTC (1400 BJT) in the early afternoon (Figs. 9a and 10a), there are three distinct west–east solenoidal circulations in the lower- to midtroposphere

of the latitude-averaged vertical cross section. These solenoidal circulations are apparently driven by the differential diabatic heating due to the difference in surface terrains with the upward branches on the highland–plateau slopes and the downward branches over the low basins, plains, or oceans. The westernmost and strongest solenoid (S1) has the westward-tilted rising branch over the eastern slope of the TP and the sinking branch over the Sichuan basin. The second solenoid in the middle (S2) has a rather shallower rising branch over the highlands along the Qinling and Wushan Mountain ranges and a more extended and broader sinking branch over the east China plains. The third solenoid (S3) has the rising branch along the coastal lands and the weak sinking branch over the nearby oceans. Each of the upward branches of the solenoids corresponds to a diurnal precipitation peak. On a larger scale, though not marked in Fig. 10a, there also exists a broader domain-wide vertical solenoid circulation (S0) across all three solenoids with the upward branch on the eastern TP and the downward branch over the plains.

At 1200 UTC (2000 BJT) in the early evening (Figs. 9b and 10b), the S0 becomes the dominant mode in the cross section with the upward motion strengthened at the eastern slope of the TP and the downward motion over most of the areas eastward except for the weak upward branch of the S2 in the lower troposphere on the eastern slope of the Qinling and Wushan Mountain ranges ( $\sim 112^{\circ}$ E). Both the upward branches of S1 and S2 continue to be associated with local diurnal precipitation maxima at this hour while the broader and stronger sinking branch over the east China plains corresponds to a broad local precipitation minimum phase in these regions at this hour. The coastal solenoid S3 is mostly absent in this early evening hour though the sinking branch over the ocean is considerably stronger than over the coastal land.

At 1800 UTC (0200 BJT) in the early morning (Figs. 9c and 10c), the nighttime vertical circulation is nearly a complete reversal of the daytime circulation at 0600 UTC (1400 BJT in Figs. 9a and 10a) with the downward branches over the highland–plateau slopes and the upward branches over the low-lying plains–basins. Consequently, strong diurnal precipitation peaks (nocturnal rainfall maxima) are observed over the Sichuan basin (part of S1) and over the east China plains (part of S2). However, according to the diurnal evolution of the rainfall shown in Fig. 8h, the nocturnal circulation pattern may be further strengthened to peaked maximum at 2100 UTC at a time when the GFS analysis is not available. On the other hand, as discussed in HZ10 and other studies (e.g., Higgins et al. 1997; Carbone and Tuttle 2008), the nocturnal precipitation peak phase over the plains is also

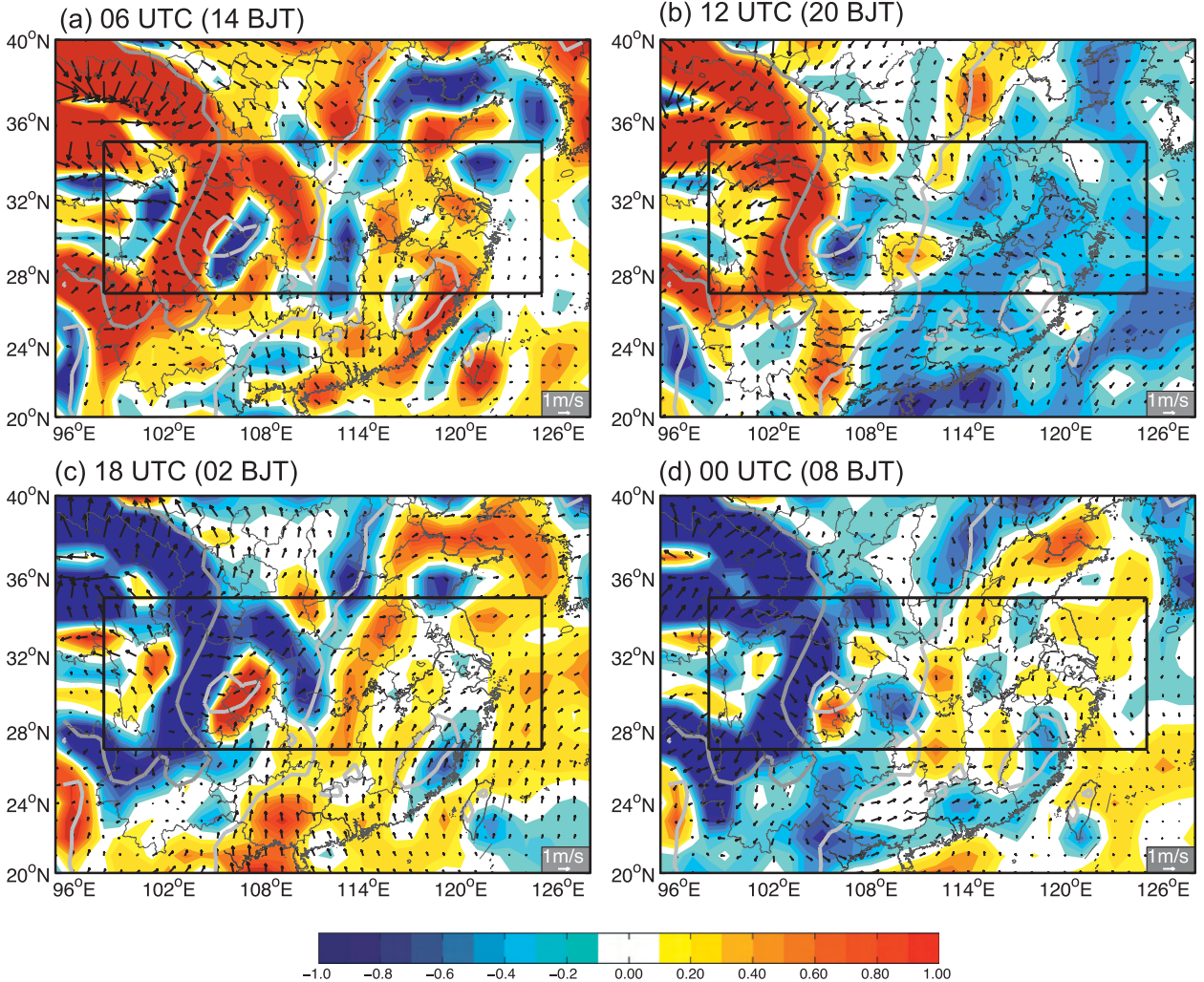


FIG. 9. Spatial distribution of the 850-hPa vertical motion derivations ( $\text{cm s}^{-1}$ , colors) and perturbation wind vectors diagnosed with the GFS analyses at (a) 0600, (b) 1200, (c) 1800, and (d) 0000 UTC averaged over the pre-meiyu period.

coincident with a developing low-level southerly jet that transports more warm moist air to this area and contributes to the enhancement of nighttime precipitation. The strongest positive anomaly of meridional wind (as an indication of the strength of the low-level jet anomaly) at 1800 UTC (0200 BJT) is indeed situated over the plains east of 115°E. Boundary layer processes associated with the reduced turbulence diffusion due to ceased daytime heating are believed to be responsible for the development of the low-level nocturnal jet (Blackadar 1957; Holton 1967).

At 0000 UTC (0800 BJT) a few hours after sunrise (Figs. 9d and 10d), the vertical circulation transitions from the nocturnal pattern in Figs. 9c and 10c to the daytime pattern in Figs. 9a and 10a, and is again dominated by the domain-scale broad solenoid (S0) as a reversal of that in Figs. 9b and 10b with the downward motion

maximized at the eastern slope of the TP and the upward motion in a broad area to its east maximized at the mid-troposphere. S1 becomes even stronger than the nocturnal phase 6 h previous as it moves eastward corresponding to the midmorning precipitation peaks in the northeastern Sichuan basin (Figs. 5b and 8), while S2 becomes weaker. Future research will conduct mesoscale reanalysis and forecast at higher spatial and temporal resolutions than GFS analysis for the region to examine in greater detail the diurnal variations of these MPS.

In summary, during the pre-meiyu period, the diurnal precipitation peak moves eastward from the eastern edge of the TP to the coastal plains in about 2 days, and the averaged propagation speed (estimated between 101° and 112°E) is approximately  $15 \text{ m s}^{-1}$  (Fig. 5b). This diurnal peak is strengthened twice in its eastward propagation, once on the eastern slope of the Qinling

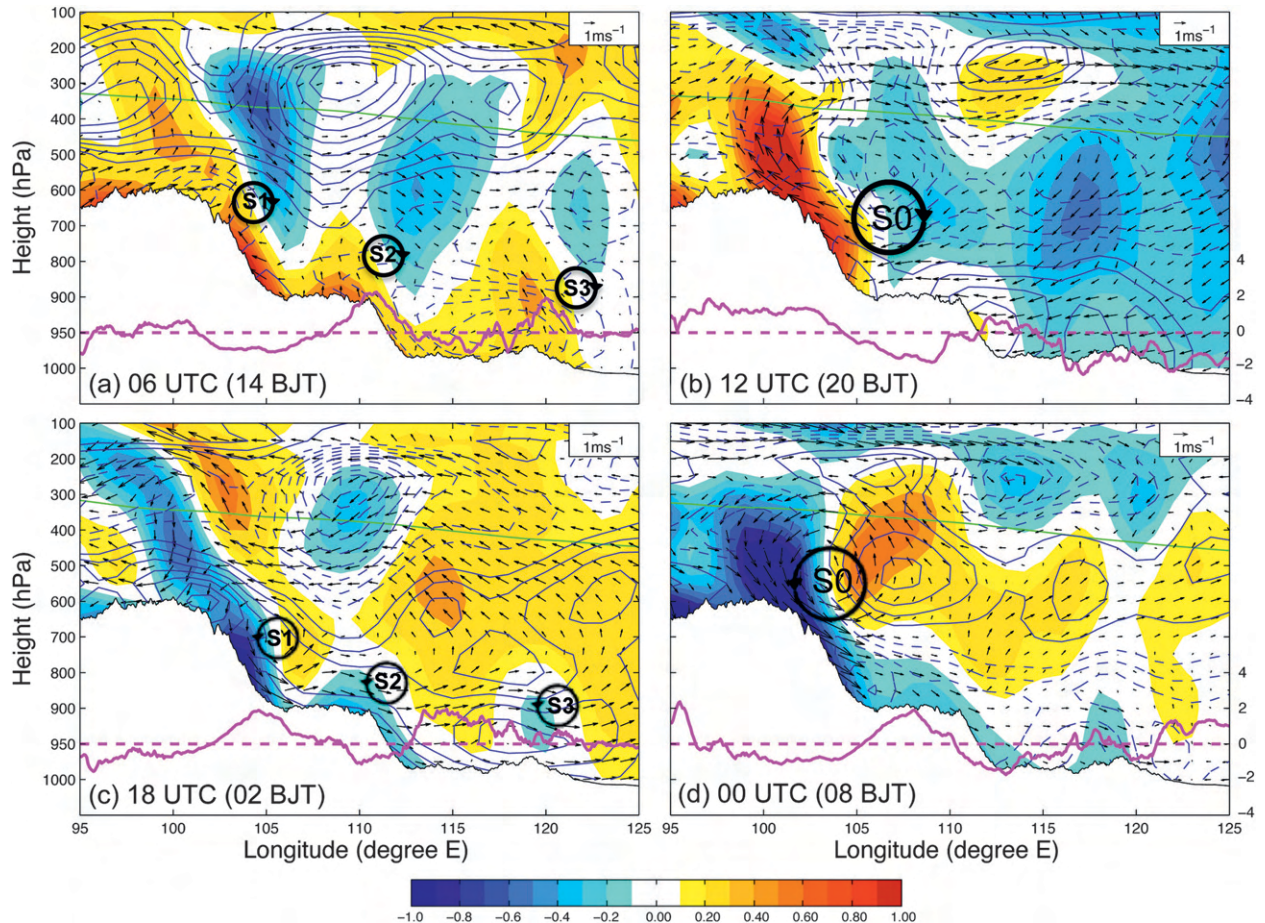


FIG. 10. Vertical profiles of the vertical motion deviations (unit:  $\text{cm s}^{-1}$ , colored), the perturbation vertical circulation vectors (zonal wind and 100 times of vertical velocity), and the perturbation meridional winds ( $0.2 \text{ m s}^{-1}$ ; solid blue, positive; dashed, negative) latitudinally averaged between  $27^\circ$  and  $35^\circ\text{N}$  diagnosed with GFS analyses at (a) 0600, (b) 1200, (c) 1800, and (d) 0000 UTC during the pre-mei-yu period. The pink solid curves show the averaged normalized diurnal precipitation deviations with the pink dashed straight line as the zero value. The black solid curves show the averaged terrain elevations. The green solid lines show that the zonal wind is equal to the mean diurnal propagation speed of  $15 \text{ m s}^{-1}$ . The S0, S1, S2, and S3 show the approximate solenoidal centers.

and Wushan Mountain ranges ( $110^\circ$ – $112^\circ\text{E}$ ), and again along the east coast ( $118^\circ$ – $120^\circ\text{E}$ ). From Figs. 8a and 9a, these two local enhancements appear to be a result of the local solenoids (S2 and S3) that are in phase with the propagating diurnal precipitation peak originating from S1 on the second and the third day, respectively. In other words, the local enhancements by S2 and S3 may have contributed substantially to the longevity and coherence of diurnal phase propagation during the pre-mei-yu period. A recent modeling study by Huang et al. (2010) on an individual event revealed that in addition to the eastern TP acting as a heat source for convection, the diurnal solenoid circulation also contributes to the longevity and propagation of episodes. Another recent study of Chen et al. (2010) also examined the diurnal variations of summertime long-duration nocturnal rainfall down the Yangtze-River Valley. They found that the diurnal clockwise rotation of the

low-tropospheric circulation might explain the eastward-delayed initiation of the long-duration nocturnal rainfall events while the upward motion belt moves eastward in time. However, both of these studies only identified the broad vertical circulation driven by the TP thermal forcing (S0) without discussing the three individual contributing solenoids (S1, S2, and S3) likely due to the even coarser spatial resolution dataset they used ( $2.5^\circ \times 2.5^\circ$  vs  $1^\circ \times 1^\circ$ ).

#### b. The mei-yu period (15 June–15 July)

During the mei-yu period (15 June–15 July), the WPSH moves northward (Fig. 3c); consequently, the primary summertime rain belt in China shifts north to the focus area and then becomes quasi-stationary over central and east China (Fig. 2c). The period-mean synoptic environment is different from what it is during the pre-mei-yu

period (Fig. 3b), as are the diurnal variations of precipitation (Figs. 4b and 5b). The red dashed box in Fig. 2c indicates the main rain belt of this period ( $30^{\circ}$ – $34^{\circ}$ N, east of  $112^{\circ}$ E). Figure 11 shows the normalized diurnal precipitation deviations at different hours during the mei-yu period. In comparison to the pre-mei-yu period, it is found that most of the diurnal variations and propagation west of  $114^{\circ}$ E are more or less similar to those in Fig. 8 while differing greatly east of  $114^{\circ}$ E. More specifically, the diurnal precipitation peak still starts in the early afternoon hours over the eastern edge of the TP, which propagates continuously eastward across the Sichuan basin and arrives at the eastern slope of the Qinling and Wushan Mountain ranges in the afternoon hours on the second day. The averaged eastward-propagation speed during this period is  $\sim 13 \text{ m s}^{-1}$  (estimated between  $101^{\circ}$  and  $111^{\circ}$ E in Fig. 5c), slightly slower than that during the pre-mei-yu period. The propagating diurnal precipitation peak weakens in the foothills of these mountain ranges (around  $114^{\circ}$ E) in the morning hours on the third day (Figs. 5c and 11h). To the east of  $114^{\circ}$ E, the diurnal peak phase front changes from north–south oriented to a northeast–southwest orientation over the plains (and more parallel to the mei-yu frontal rain belt highlighted by a red dashed box).<sup>4</sup> Coincidentally, there is also a local oscillating quasi-stationary mode (in contrast to the continuous spatial phase propagation) overlapped with elements of eastward-propagating diurnal signals from west to east. More specifically, along the mei-yu rain belt, positive anomalies of the precipitation deviation are observed in the morning hours (2100–0300 UTC or 0500–1100 BJT; Figs. 11a,b,h) and negative anomalies from the afternoon to the evening hours (0900–1500 UTC or 1700–2300 BJT; Figs. 11d–f). The diurnal precipitation variations to the south and north sides of this primary mei-yu frontal rain belt overall are similar but in a nearly opposite phase to that within the red box.

Nevertheless, there is about a 6-h phase lag between the south and north sides; the south subregion diurnal precipitation reaches a peak (minimum) around 0600–0900 UTC or 1400–1700 BJT (1800–2100 UTC or 0200–0500 BJT) while the north peaks between 1200 and 1500 UTC (2000 and 2300 BJT). The characteristics of the diurnal variations along the mei-yu frontal rain belt and adjacent areas are broadly consistent with Geng and Yamada (2007). A more complex diurnal evolution in different areas of this region is also discussed in Yu et al. (2007a).

<sup>4</sup> It is possible that there may be a resonance of speed/distance propagation among the three local MPS circulations S1–S3 and the timing of their regeneration, which was pointed by Laing et al. (2008) for their study over the African continent.

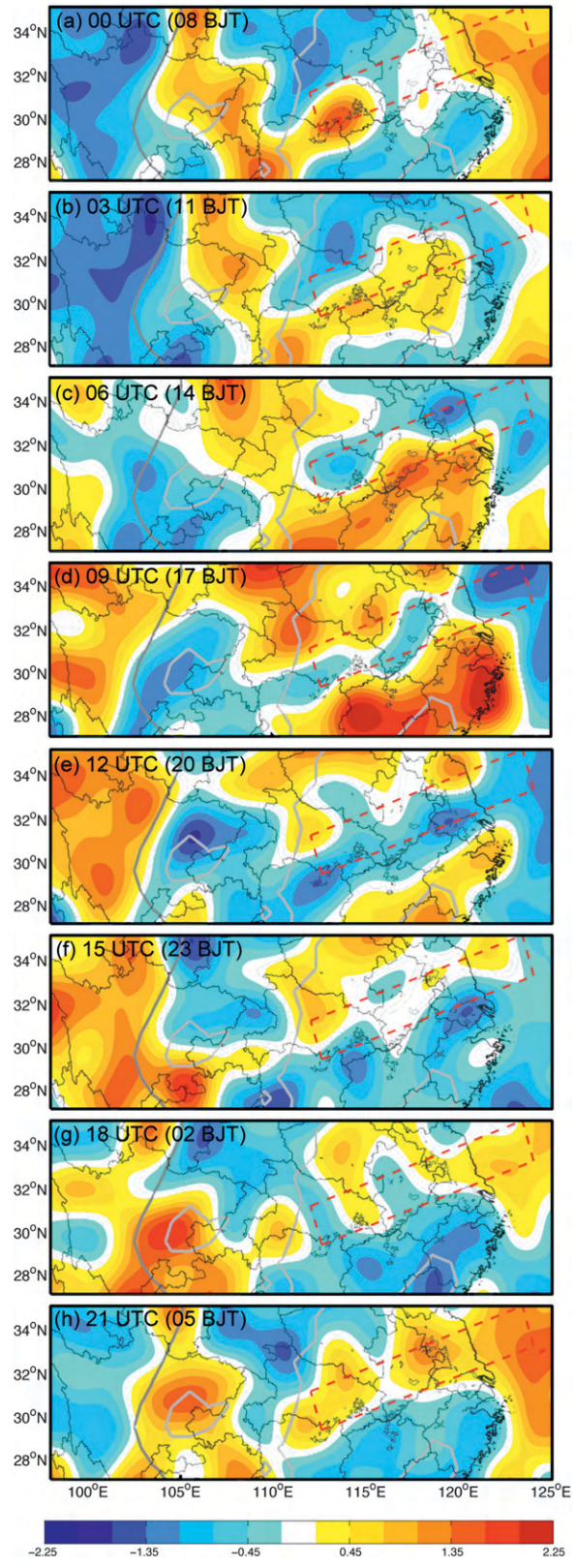


FIG. 11. As in Fig. 6, but for the mei-yu period. The red dashed box denotes the primary mei-yu front rain belt.

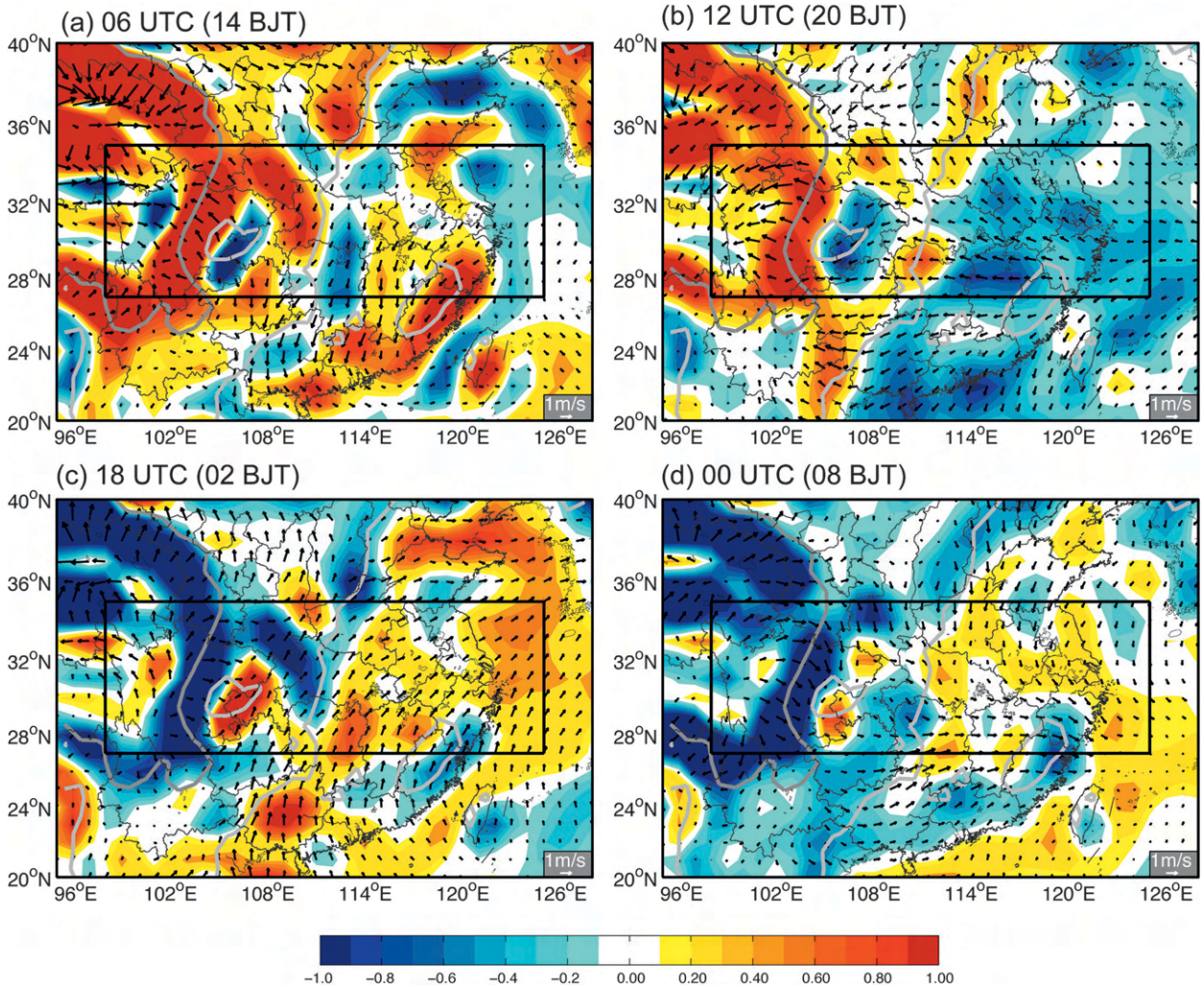


FIG. 12. As in Fig. 9, but for the mei-yu period.

Figure 12 shows the low-level (850 hPa) vertical motion deviations and perturbation wind vectors for each GFS analysis during the mei-yu period averaged over 2003–09. Figure 13 shows the corresponding latitudinally averaged vertical motions and the perturbation vertical circulation vectors along the west–east cross section. Despite differences in the details of relative size and strength, the three localized solenoidal circulations (S1–S3) as well as the domain-wide large-scale vertical circulation S0 (Figs. 12 and 13) are mostly similar in phase and location to those observed during the pre-mei-yu period (Figs. 9 and 10). Comparison of the vertical circulations between Figs. 10 and 13 suggests that the lack of clearly identifiable eastward diurnal precipitation phase propagation east of 114°E (in Figs. 5c and 11) is likely due to the presence of the strong mei-yu front precipitation that has a predominant quasi-stationary north–south diurnal oscillation as described above.

### c. The post-mei-yu period (15 July–15 August)

During the post-mei-yu period (15 July–15 August), the WPSH moves farther northward and extends more to the west (Fig. 3d), while the primary rain belt only overlaps the northern edge of the focus domain. The east China plains are now under the dominance of the quasi-stationary high pressure system resulting in an even weaker midlatitude westerly flow over the focus domain and much reduced precipitation during this period (Fig. 2d) except for occasional occurrences of tropical cyclones. Consequently, on average, the eastward propagation of the diurnal precipitation peak originating from the eastern TP is further slowed and becomes barely traceable over the plains (Figs. 5d). The averaged eastward-propagation speed during this period is  $\sim 9 \text{ m s}^{-1}$  (estimated between 102° and 110°E in Fig. 5d), which is substantially slower than that during the previous two periods. The diurnal

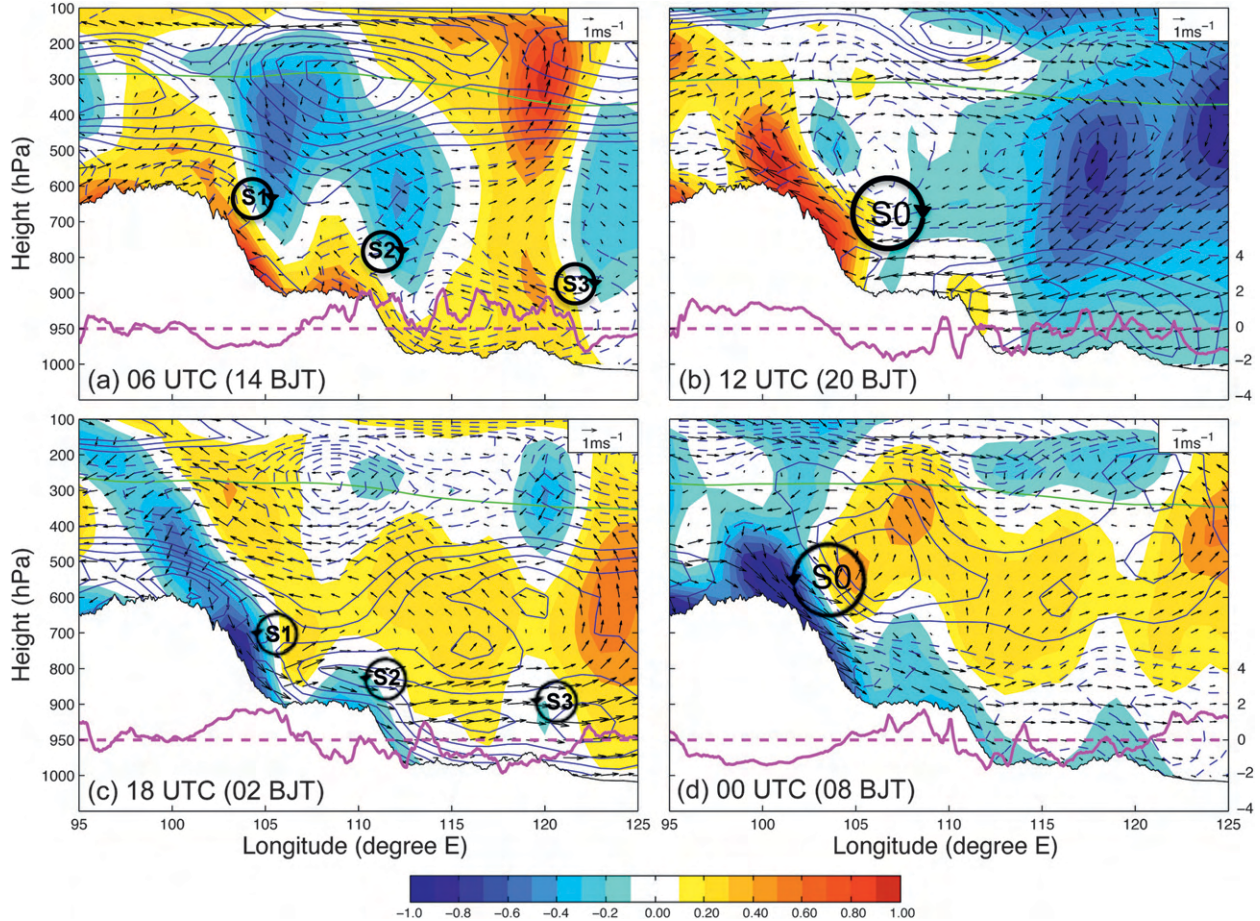


FIG. 13. As in Fig. 10, but for the mei-yu period with the green solid lines showing the zonal wind is equal to the mean diurnal propagation speed of  $13 \text{ m s}^{-1}$  during the mei-yu period.

precipitation, averaged latitudinally over the central China highlands and east China plains during this period, has a dominant peak in the late afternoon and a minimum in the morning with little or no spatial phase propagation in the latitudinal average (Fig. 5d).

However, this latitudinal average apparently does not capture some of the relatively weaker and less coherent diurnal propagations that are not strictly oriented north-south as illustrated in the normalized diurnal precipitation deviations at different hours (Fig. 14). For example, a secondary diurnal precipitation peak originating at top of the Taihangshan Mountain ranges in north China in the early afternoon (Fig. 14c) propagates southeastward into this study's focus domain. This secondary diurnal peak reaches the northern plain area of the focus domain in the later evening and early morning hours corresponding to secondary nocturnal precipitation maxima in this region (Figs. 14f–h). Evolution of this secondary peak is similar to HZ10 where possible mechanisms for the nocturnal rainfall maximum were discussed in details.

On the other hand, the spatial propagation of the diurnal precipitation peak from the TP to the highlands (Fig. 14) remains more or less similar to the previous two periods (Figs. 8 and 11). Figure 15 shows the 850-hPa vertical motions deviations and perturbation wind vectors at each GFS analysis during the post-mei-yu period averaged over 2003–09. Figure 16 shows the corresponding latitudinally averaged vertical motions and the perturbation vertical circulation vectors along the west–east cross section. Both the low-level anomaly plots and the latitudinally averaged longitude–height diagrams in Figs. 15 and 16 are also similar to those of the previous periods that show three local vertical circulations (S1–S3) most discernible at 0600 and 1800 UTC (1400 and 0200 BJT) as well as a domain-wide broader-scale mountain–plains solenoid (S0) most apparent at 0000 and 1200 UTC (0800 and 2000 BJT). Again, the detailed diurnal phase variations and propagation of these solenoids cannot be fully resolved in the rather coarse temporal resolution of the GFS analysis.

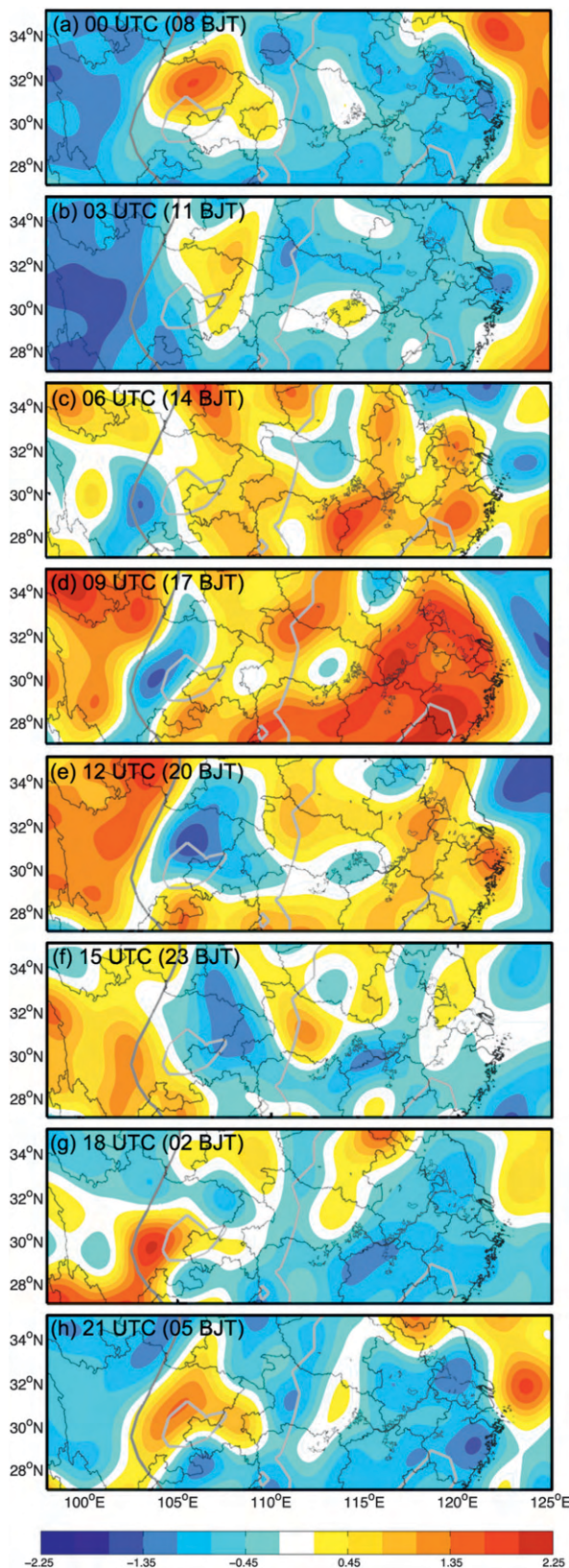


FIG. 14. As in Fig. 6, but for the post-mei-yu period.

## 5. Discussion of the difference in diurnal variations during different periods

Analyses of the diurnal variation during different summer months in the previous sections show that 1) there are strong diurnal variations in the summertime precipitation over the focus domain to the east of the TP; 2) these diurnal precipitation cycles are strongly associated with several thermally driven regional mountain-plains solenoids due to the differential heating between the TP, the highlands, the plains, and the ocean; 3) the diurnal cycles differ greatly from region to region and during different rainy periods. In particular, there is substantial difference in the propagation speed and eastward extent of the dominant diurnal precipitation peak that is originating from the TP. This diurnal peak has a faster (slower) eastward-propagation speed, more (less) coherent propagation duration, and thus covers the longest (shortest) distance to the east during the pre-mei-yu (post-mei-yu) period than that during the mei-yu period.

What causes the difference in the propagation speed and the eastward extent of this dominant diurnal precipitation peak originating from the TP? The above analysis suggests that even though the diurnal precipitation cycles are strongly associated with several mountain-plains solenoids, these regional solenoidal circulations between different periods are more or less similar in the coarse temporal resolution GFS analysis whose difference is not enough to explain the difference in the diurnal propagation during different periods.

More likely mechanisms to explain the propagation difference are the difference in the mean midlatitude steering-level westerly flow and the difference in positioning and strength of the WPSH during different periods (Fig. 3). The steering level is defined at the level where the phase propagation speed of the features equals the speed of the background flow. Over the TP and the adjacent highlands, the steering level is at approximately 500–350 hPa and over the plains at approximately 600–450 hPa. Figure 17 further shows the time–latitude diagrams of averaged midtropospheric zonal winds diagnosed with the GFS analyses from 15 May to 15 August averaged over two subdomains, one between 102° and 110°E for pressure levels between 500 and 350 hPa (Fig. 17a), and the other between 112° and 120°E for between 600 and 450 hPa (Fig. 17b). Indeed, consistent with the gradual decrease in the eastward-propagation speed of the diurnal precipitation peak, the averages of the zonal winds in the midtroposphere over both subdomains are decreasing with time and latitude. The southern parts of both subdomains begin to see the reversal of zonal winds at the start of the post-mei-yu period while nearly one-third of the domain is under the easterlies toward the end of the

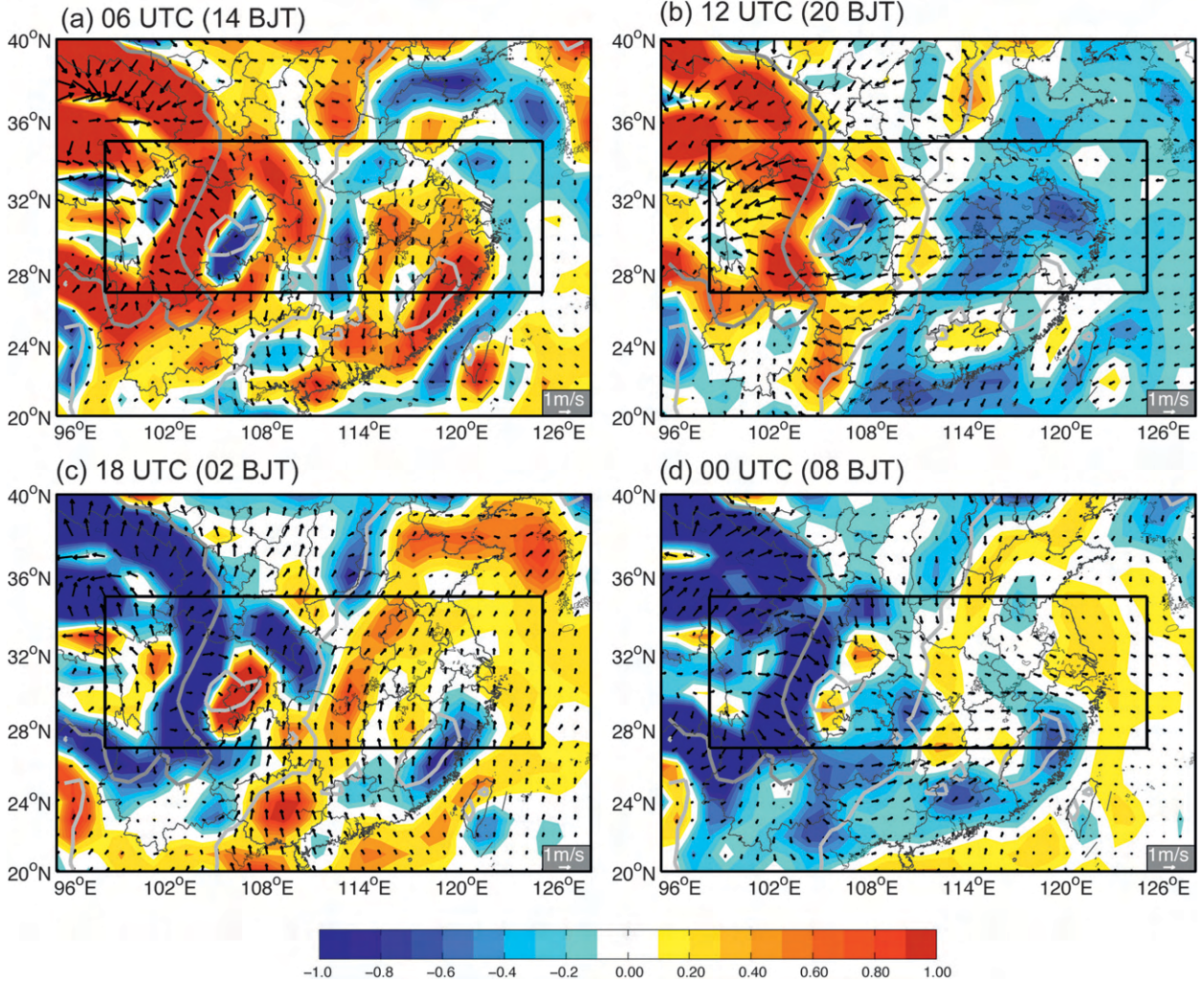


FIG. 15. As in Fig. 9, but for the post-mei-yu period.

post-mei-yu period. The decrease of the westerly flow throughout these summer months and the emergence of the easterly flow will likely lead to the decrease in the eastward propagation of the diurnal precipitation peak and prevent it from advancing farther eastward to the plains during the later months of the summer. As discussed in section 3, the decrease in the midtropospheric zonal flow is due to the strengthening of the WPSH, which shifts north and protrudes more inland at the start of the mei-yu period and again at the start of the post-mei-yu period (Fig. 3). Note that the difference in the eastward propagation of the diurnal rainfall signals during different summer months was also noted in Wang et al. (2004, 2005, 2011) though without explanation of the difference.

## 6. Conclusions

This study explores the diurnal variations of the warm-season precipitation to the east of the TP over China

using the high-resolution CMORPH precipitation data and the GFS gridded analyses during mid-May to mid-August of 2003–09. Warm-season rainfalls account for most of the total annual precipitation in this focus area and thus have very important impacts on the water cycles and climate of the region that includes several of the most densely populated cities and provinces of China. Also investigated are the differences in diurnal variations and propagation among the three different month-long periods: the pre-mei-yu period (15 May–15 June), the mei-yu period (15 June–15 July), and the post-mei-yu period (15 July–15 August).

Averaged over the entire 3-month period, it is found that the local peak phase of the diurnal precipitation usually begins in the mid- to late afternoon on the eastern edge of the TP, which subsequently propagates eastward and downslope at an average speed of  $\sim 13 \text{ m s}^{-1}$ . The primary diurnal precipitation peak reaches the Sichuan basin and

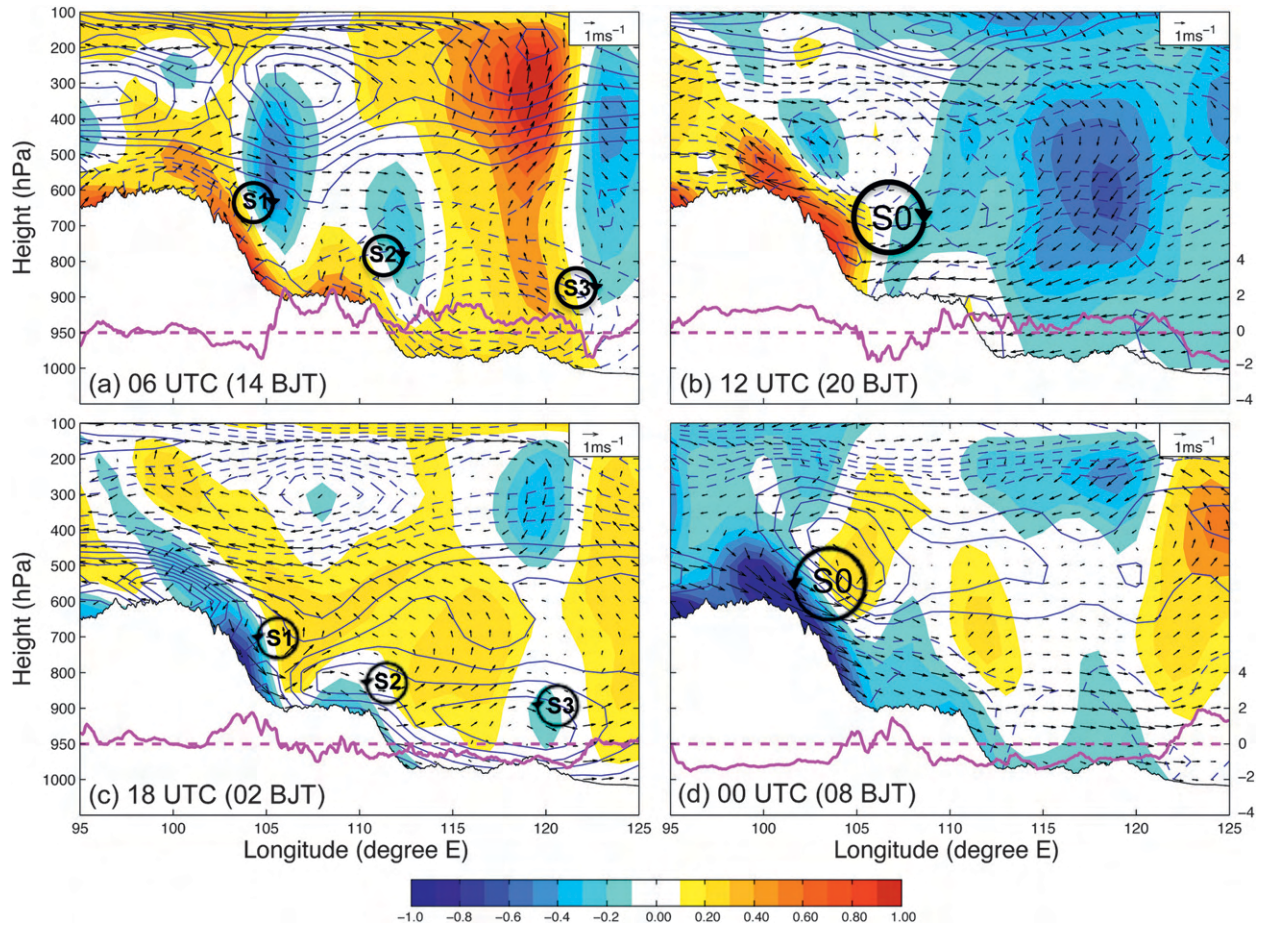


FIG. 16. As in Fig. 10, but for the post-meiyu period.

adjacent highlands to its east around midnight and the early morning hours, and coincides with well-observed nocturnal rainfall maximum in this region. The diurnal precipitation maximum continues to move eastward at a slightly slower phase speed and gradually weakens in relative magnitude that may coexist and interact with other diurnally varying precipitation modes. The most dominant diurnal precipitation peak persistent over all land areas to the east of  $108^{\circ}\text{E}$  occurs in the midafternoon (with maximum solar heating), while a secondary propagating maximum, as a continuation of the signal from the TP and the Sichuan basin, peaks around midnight on the second day over the east China plains. These diurnal precipitation cycles are strongly associated with several thermally driven regional mountain–plains solenoids due to the differential heating between the plateaus, the highlands, the plains, and the ocean.

It is also found that the diurnal cycles differ greatly from region to region and in the propagation speed and eastward extent during different rainy periods. This diurnal peak originating from the eastern edge of the TP

during the pre-meiyu period propagates eastward at an average velocity of  $\sim 15 \text{ m s}^{-1}$ . It reaches all the way to the east coast on the third day ( $\sim 45 \text{ h}$ ) covering a distance of  $\sim 2000 \text{ km}$ . The average eastward speed of this diurnal precipitation peak is  $\sim 13 \text{ m s}^{-1}$  during the meiyu period, which is clearly traceable only to the western edge of the plains ( $\sim 114^{\circ}\text{E}$ ) in  $\sim 32 \text{ h}$ . The post-meiyu period features the slowest propagation speed of  $\sim 9 \text{ m s}^{-1}$ , which is mostly confined to the west of  $113^{\circ}\text{E}$  and barely reaches the plains.

The differences in the mean midlatitude westerly flow and in the positioning and strength of the WPSH during different periods are the key factors in explaining the difference in the propagation speed and the eastward extent of this dominant diurnal precipitation cycle. Compared with the other two periods, the WPSH during the pre-meiyu period is situated over the ocean that is the farthest south and east while the midlatitude westerly flow is the strongest and farthest south resulting in the highest eastward-propagation speed of the diurnal precipitation peak that also has the most eastward extent. The opposite is true for the post-meiyu period while the

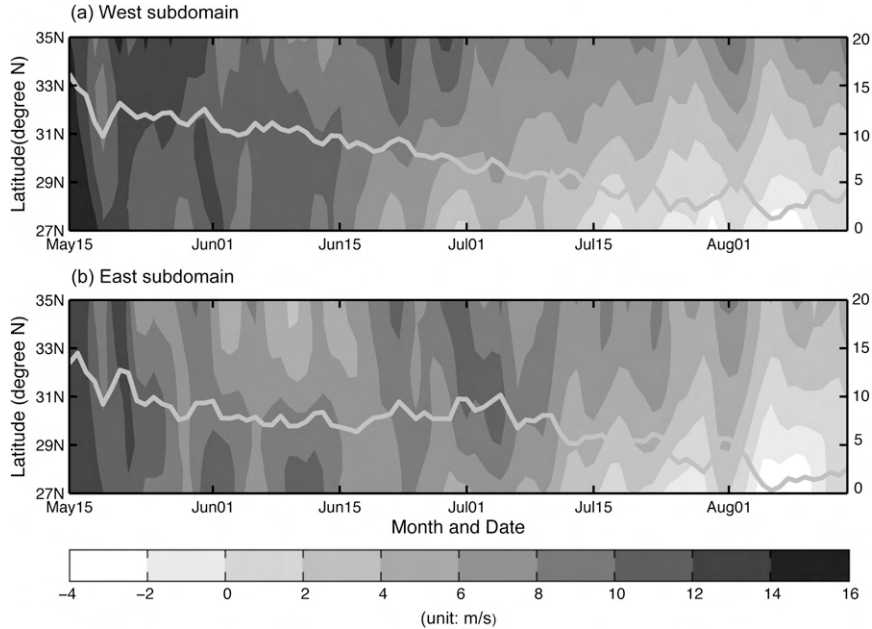


FIG. 17. Time–latitude diagrams of averaged midtropospheric zonal wind speed (shaded;  $\text{m s}^{-1}$ ) diagnosed with the GFS analyses from 15 May to 15 Aug over (a) the west subdomain averaged between  $102^\circ$  and  $110^\circ\text{E}$  and for pressure levels between 500 and 350 hPa, and (b) the east subdomain averaged between  $112^\circ$  and  $120^\circ\text{E}$  and for pressure levels between 600 and 450 hPa. The gray solid curves show the area-mean zonal wind speed ( $\text{m s}^{-1}$ ) averaged over (a) the west subdomain ( $27^\circ$ – $35^\circ\text{N}$ ,  $102^\circ$ – $110^\circ\text{E}$ ) and (b) the east subdomain ( $27^\circ$ – $35^\circ\text{N}$ ,  $112^\circ$ – $120^\circ\text{E}$ ).

diurnal cycle during the mei-yu period is in between the two periods and this also is closest to the three-month warm-season mean.

Similar to what discussed in HZ10, the following mechanisms may be responsible for the nocturnal precipitation maximum over the east China plains. These nocturnal precipitation peaks may have been initiated first or enhanced on the eastern slopes of the TP during peak solar heating hours, which subsequently move eastward and reach the plains at the nighttime following the midtropospheric mean flow. The nocturnal precipitation peaks over the plains could also be due to the local initiation or enhancement of precipitation by the upward branch of a mountain–plains solenoid induced by differential heating between the TP and the highlands or between the highlands and the plains. The nighttime precipitation peaks can be initiated or enhanced by a nocturnal low-level jet over the plains, which brings warmer, moister air to the area during the nighttime. Future studies will examine the respective contributions different mechanisms, as performed in Trier et al. (2006, 2010) for the continental United States, or through high temporal and spatial resolutions regional-scale reanalysis that better resolves the evolution of the regional mountain–plains solenoids and their impacts on the diurnal precipitation variations over this region.

**Acknowledgments.** We are grateful for Pingping Xie and Soo-Hyun Yoo for providing the CMORPH dataset and Chris Slocum for proofreading. The authors are also thankful for the data and computing support provided by Huizhong He and Yonghui Weng. This is part of the first author's Ph.D. dissertational research at Nanjing University cosponsored by Professors Yunqi Ni and Xiuqun Yang. This research was jointly sponsored by CMA project “Study for Short-Time Prediction Technology of Meso-Scale Severe Weather” (GYHY201006003) and NSF Grant ATM-0904635.

## REFERENCES

- Asai, T., S. Ke, and Y.-M. Kodama, 1998: Diurnal variability of cloudiness over East Asia and the Western Pacific Ocean as revealed by GMS during the warm season. *J. Meteor. Soc. Japan*, **76**, 675–684.
- Blackadar, A. K., 1957: Boundary layer wind maxima and their significance for the growth of nocturnal inversions. *Bull. Amer. Meteor. Soc.*, **38**, 283–290.
- Carbone, R. E., and J. D. Tuttle, 2008: Rainfall occurrence in the U.S. warm season: The diurnal cycle. *J. Climate*, **21**, 4132–4146.
- , —, D. Ahijevych, and S. B. Trier, 2002: Inferences of predictability associated with warm season precipitation episodes. *J. Atmos. Sci.*, **59**, 2033–2056.
- Chen, G., W. Sha, and T. Iwasaki, 2009: Diurnal variation of precipitation over southeastern China: Spatial distribution and

- its seasonality. *J. Geophys. Res.*, **114**, D13103, doi:10.1029/2008JD011103.
- Chen, H., R. Yu, J. Li, W. Yuan, and T. Zhou, 2010: Why nocturnal long-duration rainfall presents an eastward-delayed diurnal phase of rainfall down the Yangtze River Valley. *J. Climate*, **23**, 905–917.
- Dai, A., 2001: Global precipitation and thunderstorm frequencies. Part II: Diurnal variations. *J. Climate*, **14**, 1112–1128.
- , F. Giorgi, and K. E. Trenberth, 1999: Observed and model simulated precipitation diurnal cycle over the contiguous United States. *J. Geophys. Res.*, **104**, 6377–6402.
- Fitzjarrald, D. R., R. K. Sakai, O. L. L. Moraes, R. Cosme de Oliveira, O. C. Acevedo, M. J. Czikowsky, and T. Beldini, 2008: Spatial and temporal rainfall variability near the Amazon-Tapajós confluence. *J. Geophys. Res.*, **113**, G00B11, doi:10.1029/2007JG000596.
- Geng, B., and H. Yamada, 2007: Diurnal variations of the Meiyu/Baiu rain belt. *SOLA*, **3**, 61–64.
- He, H., and F. Zhang, 2010: Diurnal variations of warm-season precipitation over Northern China. *Mon. Wea. Rev.*, **138**, 1017–1025.
- Higgins, R. W., Y. Yao, E. S. Yarosh, J. E. Janowiak, and K. C. Mo, 1997: Influence of the Great Plains low-level jet on summertime precipitation and moisture transport over the central United States. *J. Climate*, **10**, 481–507.
- Hirose, M., and K. Nakamura, 2005: Spatial and diurnal variation of precipitation systems over Asia observed by the TRMM Precipitation Radar. *J. Geophys. Res.*, **110**, D05106, doi:10.1029/2004JD004815.
- Hirpa, F. A., M. Gebremichael, and T. Hopson, 2010: Evaluation of high-resolution satellite precipitation products over very complex terrain in Ethiopia. *J. Appl. Meteor. Climatol.*, **49**, 1044–1051.
- Holton, J. R., 1967: The diurnal boundary layer wind oscillation above sloping terrain. *Tellus*, **19**, 199–205.
- Huang, H. L., C. C. Wang, G. T. J. Chen, and R. E. Carbone, 2010: The role of diurnal solenoidal circulation on propagating rainfall episodes near the eastern Tibetan Plateau. *Mon. Wea. Rev.*, **138**, 2975–2989.
- Joyce, R. J., J. E. Janowiak, P. A. Arkin, and P. Xie, 2004: CMORPH: A method that produces global precipitation estimates from passive microwave and infrared data at high spatial and temporal resolution. *J. Hydrometeor.*, **5**, 487–503.
- Koch, S. E., F. Zhang, M. L. Kaplan, Y.-L. Lin, R. Weglarz, and C. M. Trexler, 2001: Numerical simulations of a gravity wave event over CCOPE. Part III: The role of a mountain-plains solenoid in the generation of the second wave episode. *Mon. Wea. Rev.*, **129**, 909–933.
- Kurosaki, Y., and F. Kimura, 2002: Relationship between topography and daytime cloud activity around Tibetan Plateau. *J. Meteor. Soc. Japan*, **80**, 1339–1355.
- Laing, A. G., R. E. Carbone, V. Levizzani, and J. D. Tuttle, 2008: The propagation and diurnal cycles of deep convection in northern tropical Africa. *Quart. J. Roy. Meteor. Soc.*, **134**, 93–109.
- Levizzani, V., F. Pinelli, M. Pasqui, S. Melani, A. G. Laing, and R. E. Carbone, 2010: A 10-year climatology of warm-season cloud patterns over Europe and the Mediterranean from Meteosat IR observations. *Atmos. Res.*, **97**, 555–576.
- Liang, X.-Z., L. Li, A. Dai, and K. E. Kunkel, 2004: Regional climate model simulation of summer precipitation diurnal cycle over the United States. *Geophys. Res. Lett.*, **31**, L24208, doi:10.1029/2004GL021054.
- Lin, Y., and F. Zhang, 2008: Tracking mesoscale gravity waves in baroclinic jet-front systems. *J. Atmos. Sci.*, **65**, 2402–2415.
- Pereira Filho, A. J., R. E. Carbone, J. E. Janowiak, P. Arkin, R. Joyce, R. Hallak, and C. G. M. Ramos, 2010: Satellite rainfall estimates over South America—Possible applicability to the water management of large watersheds. *J. Amer. Water Resour. Assoc.*, **46** (2), 344–360.
- Shen, Y., A. Xiong, Y. Wang, and P. Xie, 2010: Performance of high-resolution satellite precipitation products over China. *J. Geophys. Res.*, **115**, D02114, doi:10.1029/2009JD012097.
- Tao, S. Y., 1980: *Heavy Rainfalls in China* (in Chinese). Science Press, 225 pp.
- , and L.-X. Chen, 1987: A review of recent research on the East Asian summer monsoon in China. *Monsoon Meteorology*, C.-P. Chang and T. N. Krishnamurti, Eds., Oxford University Press, 60–92.
- Trier, S. B., C. A. Davis, D. A. Ahijevych, M. L. Weisman, and G. H. Bryan, 2006: Mechanisms supporting long-lived episodes of propagating nocturnal convection within a 7-day WRF model simulation. *J. Atmos. Sci.*, **63**, 2437–2461.
- , —, —, —, and —, 2010: Environmental controls on the simulated diurnal cycle of warm-season precipitation in the continental United States. *J. Atmos. Sci.*, **67**, 1066–1090.
- Tripoli, G. J., and W. R. Cotton, 1989: Numerical study of an observed orogenic mesoscale convective system. Part II: Analysis of governing dynamics. *Mon. Wea. Rev.*, **117**, 305–328.
- Tuttle, J. D., R. E. Carbone, and P. A. Arkin, 2008: Comparison of ground-based radar and geosynchronous satellite climatologies of warm-season precipitation over the United States. *J. Appl. Meteor. Climatol.*, **47**, 3264–3270.
- Wang, C. C., G. T. J. Chen, and R. E. Carbone, 2004: A climatology of warm-season cloud patterns over east Asia based on GMS infrared brightness temperature observations. *Mon. Wea. Rev.*, **132**, 1606–1609.
- , —, and —, 2005: Variability of warm-season cloud episodes over east Asia based on GMS infrared brightness temperature observations. *Mon. Wea. Rev.*, **133**, 1478–1500.
- , H. L. Huang, J. L. Li, T. M. Leou, and G. T. J. Chen, 2011: An evaluation of the performance of the CWB NFS model for warm-season rainfall distribution and propagation over the East Asian continent. *Terr. Atmos. Oceanic Sci.*, **22**, 49–69, doi:10.3319/TAO.2010.07.13.01(A).
- Xie, S. P., H. Xu, N. H. Saji, and Y. Wang, 2006: Role of narrow mountains in large-scale organization of Asian monsoon convection. *J. Climate*, **19**, 3420–3429.
- Xu, W., and E. J. Zipser, 2011: Diurnal variations of precipitation, deep convection and lightning over and east of the eastern Tibetan Plateau. *J. Climate*, **24**, 448–465.
- Yang, G.-Y., and J. Slingo, 2001: The diurnal cycle in the tropics. *Mon. Wea. Rev.*, **129**, 784–801.
- Yang, S., and E. A. Smith, 2006: Mechanisms for diurnal variability of global tropical rainfall observed from TRMM. *J. Climate*, **19**, 5190–5226.
- Yu, R., T. Zhou, A. Xiong, Y. Zhu, and J. Li, 2007a: Diurnal variations of summer precipitation over contiguous China. *Geophys. Res. Lett.*, **34**, L01704, doi:10.1029/2006GL028129.
- , Y. Xu, T. Zhou, and J. Li, 2007b: Relation between rainfall duration and diurnal variation in the warm season precipitation over central eastern China. *Geophys. Res. Lett.*, **34**, L13703, doi:10.1029/2007GL030315.
- Zhang, F., and S. E. Koch, 2000: Numerical simulation of a gravity wave event observed during CCOPE. Part II: Wave generation by an orographic density current. *Mon. Wea. Rev.*, **128**, 2777–2796.